POLITECNICO DI TORINO

Corso di Laurea Magistrale in
Ingegneria Energetica e Nucleare

Tesi di Laurea Magistrale

Numerical analysis of the thermal effects of a runaway electron event on EU DEMO plasma facing components

Relatori

Prof.ssa Laura Savoldi

Prof. Fabio Subba

Candidato

Gianluca Ragno

ANNO ACCADEMICO 2018 – 2019

A mia nonna

Abstract

An important issue in the design of tokamak divertors is to deal with high energy fluxes carried by runaway electron beams generated inside the plasma during disruption events. These beams hit the Plasma Facing Components (PFCs), first wall and divertor, which must be designed in order to withstand the consequent loads, that could otherwise cause phenomena such as erosion or melting, followed by a LOCA (Loss Of Cooling Accident).

With the use of the Monte Carlo code FLUKA, the distribution profile of energy deposited by runaway electrons in PFCs has been assessed by ENEA, considering all the possible reactions derived by the collision of the particles inside the materials.

The scope of the present work is to compute the temperature patterns in the EU DEMO divertor and first wall, in order to forecast the presence of one of the unwanted phenomena, starting from the energy profiles computed by ENEA.

In first place, all the assumptions made and all the data used to set up the model in the FE solver Freefem++ are illustrated: the choice of the energy deposited and its duration, together with the correlations used for the heat transfer and the ones used for the thermal properties of the materials.

At the end, the computed results are highlighted: the analysis has confirmed that, for both the components, large melting can occur, requiring their replacement in case of runaway electron events, but more catastrophic events (as LOCA) are not expected.

This work constitutes a good starting point for the analysis of the effects of disruptions in DEMO, which could affect the design of plasma facing components, in order to minimize the maintenance costs of the reactor.

Contents

List of Tables

List of Figures

Chapter 1

Introduction

1.1 Magnetic confinement for fusion reactors

Nowadays nuclear fusion represents one of the most promising options in order to face the energy problem in the world. Many research activities are trying to demonstrate that this source can be used in order to produce electricity safely. [1] [2]

Fusion is the process that drives the energy production in the stars. It is a reaction in which nuclei of 2 or more atoms join together, overcoming the electromagnetic repulsion, and generating a heavier atom, whose mass is lower than the sum of the masses of the reactants, and one or more neutrons with a large amount of energy. The most promising fusion reaction is between two hydrogen isotopes: deuterium (D) and tritium (T)

$$D + T \rightarrow^4 He + n(Q = 17.6\ MeV)$$

the energy produced in the reaction is 14.1 MeV kinetic energy of the neutrons and 3.5 MeV energy of alpha particles heating the plasma. The main advantage of this reaction is the lowest activation energy among all the fusion reactions, allowing to reach lower temperatures. The main issue is the confinement of high-energy neutrons. [3] [4]

In order for the reaction to take place, the nuclei must have energy sufficient to overcome the repulsive Coulomb force between each other. Such condition can

be reached only at very high temperatures, in the range $10^7 \div 10^8\ K$, when the gas exists in the state of plasma with a balanced number of ions and electrons. [5] [6]

Fusion plasma behaviour is dominated by long-range electric and magnetic fields, as opposed to short-range Coulomb collisions. A major consequence of this behaviour is that a plasma is an exceptionally good conductor of electricity (its electrical conductivity is about 40 times larger than that of copper). This is due to high temperatures and low particle densities entailing very low resistance to the current flow.
Among the issues for the development of a reliable nuclear fusion reactor we can quote:

- the plasma heating
- the plasma confinement

The heating system is fundamental to guarantee that the gas reaches the temperature required to exist in the state of plasma. The gas is injected into the plasma chamber, where a suitable pumping system is able to provide vacuum. Then, the heat can be provided by means of high-energy neutral particle beams (α) injected into the chamber or using RF systems. Once reached the required temperature, the fusion reaction can be self sustaining if the following relation is satisfied:

$$n\tau_E T \geq 3 \cdot 10^{21} keV/m^3$$

where n is the density of particles and τ_E is the energy confinement time. This condition is called plasma ignition. If it is satisfied (in case the reactor works ideally) no more external power is required to heat the plasma. However it would be difficult to control the reaction and the dynamics would be completely turbulent and stochastic. So it's preferred the use of an auxiliary power for the heating. [6]
Research studies have demonstrated that the best configuration of the chamber to provide a good confinement of the plasma and avoid losses, is a torus.
Thanks to the high conductivity of plasma, its confinement can be provided by a magnetic field, obtained by a combination of three different components, as shown in figure 1.1:

- toroidal: provided by a series of coils, aimed at forcing the motion of the plasma particles along the torus
- vertical: provided by a central solenoid, in order to control the position of the plasma
- poloidal: generated inside the plasma, ensuring its equilibrium

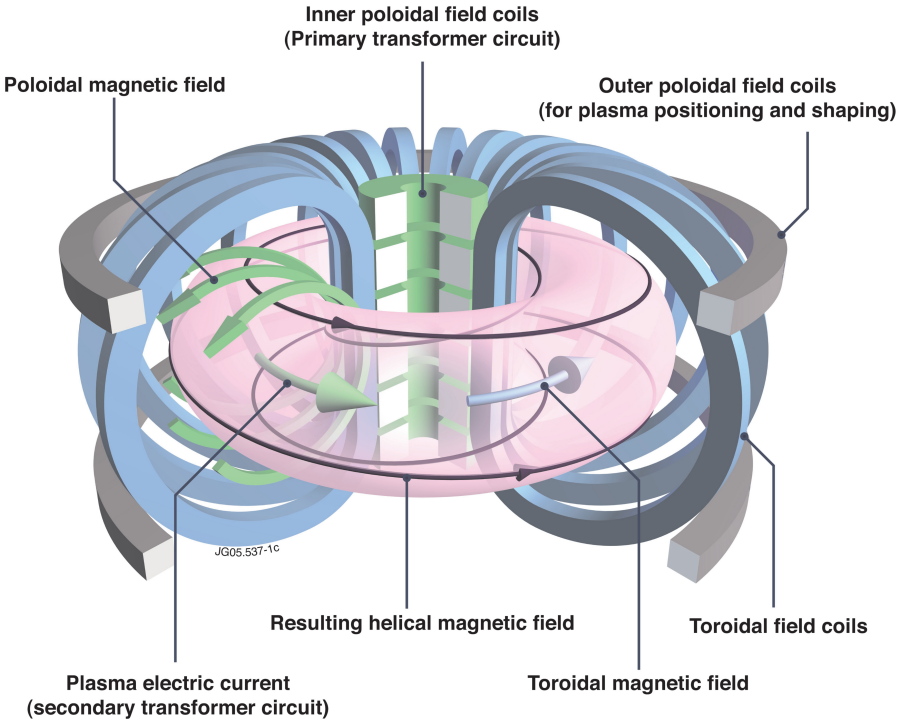

Figure 1.1: Magnetic fields for plasma confinement [7]

The sum of these contributions results in helical trajectories of the charged particles. [8] [6]
The inducted current in plasma in toroidal direction generates an electric field with a component parallel to B. This electric field, even if it is small, can cause the acceleration of a population of electrons in the plasma from modest velocity (compared to c) to relativistic speeds. These particles are named runaway electrons (RAE) (see figure 1.2).

Runaways tends to escape from the plasma striking the first wall of the reactor and causing damages to the materials due to their high energy.

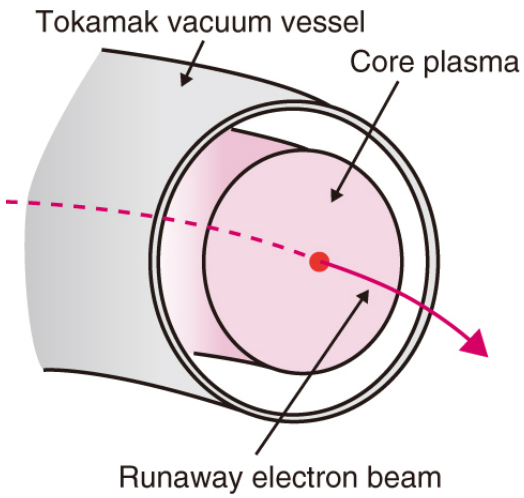

Figure 1.2: RAE beam [9]

The runaway population is a very strong function of number density of particles (n) and a practical way to minimize the effects of these electrons is to operate at sufficiently high n. This condition can be easily satisfied in steady-state condition, but during start-up n tends to be lower.

The best configuration of fusion reactors, able to guarantee all the characteristics for a good confinement of the plasma and to satisfy all the requirements for a good stability of the plasma condition, is the tokamak.
The two main projects of fusion reactors with a tokamak configurations are the ITER and the DEMO. [5]
ITER (International Thermonuclear Experimental Reactor) aims at demonstrating that fusion plasma can support a steady fusion reaction for a sufficiently long time.[10]
DEMO (DEMOnstrating fusion power reactor) aims at demonstrating that electric power can be produced starting from a fusion reaction.[11]
The main components of a tokamak reactor are [6]:

- toroidal plasma chamber, where the fusion reaction occurs (see previous sections)
- superconducting magnets, aimed at providing plasma confinement
- first wall (FW) of the blanket, which main function is the extraction of the heat radiated by the plasma [12] [13]
- breeding blanket, which has three functions: extraction of the heat radiated and carried by particles hitting the FW, by means of a suitable cooling system; breeding of the Tritium needed for the fusion reaction, in order to achieve its self-sufficiency; shielding of the magnets from the neutrons leaving the plasma [12] [13]
- divertor, aimed to extract the ashes produced by fusion reaction, in order to avoid the poisoning of the plasma and to extract the hat radiated from the plasma [14]

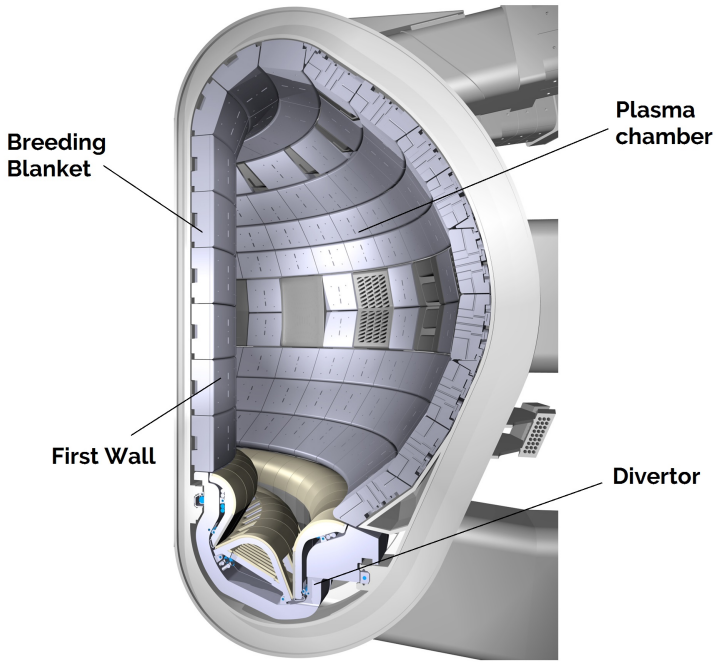

Figure 1.3: View of a tokamak section (adapted from [15])

The most critical components, which are now under investigation, are the plasma facing components (PFCs): the divertor and the first wall.
These elements are exposed to high heat loads, due to the contact with plasma, which can strongly increase when runaway electrons are generated.
Large runaway currents are expected to be formed during the current quench phase of disruptions in the reactor. During the termination phase of the disruption, when the plasma current and the runaway electrons are lost, conversion of the magnetic energy of the runaway plasma into runaway kinetic energy can occur. Runaway electrons usually deposit their energy in very short pulses and on localized areas of these components, leading to a reduction of their lifetime and, in some cases, requiring their replacement due to melting.[16] [17]

The divertor target plates are the most thermally loaded in-vessel components because of plasma radiation and neutron irradiation. A feasible design has been

developed, taking into account the high heat fluxes on the plasma facing side. DEMO divertor is composed of 54 separable cassettes, made of tungsten with double-layer cooling tubes [18] [19].

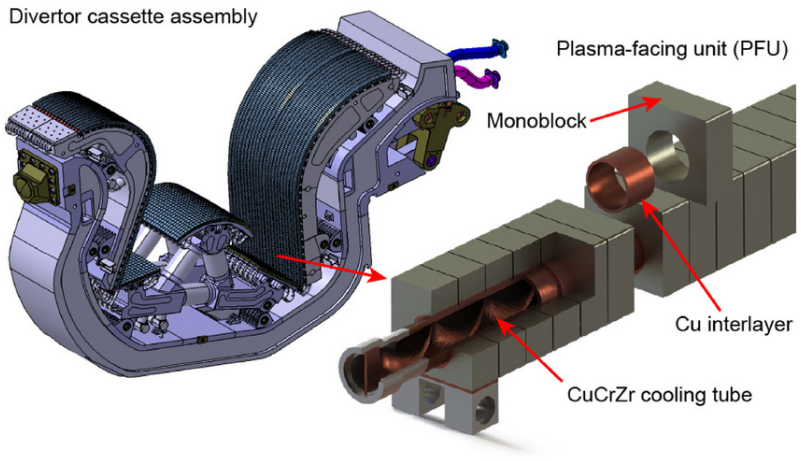

Figure 1.4: Divertor cassette of DEMO reactor [20]

The first wall (FW) is the plasma facing part of the DEMO breeding blanket. Its main function is extracting heat due to heat loads. It is mainly made of EUROFER97, with an armour of tungsten on the plasma facing area, ans it is cooled with a water system independent from the one of the breeding blanket module [21].

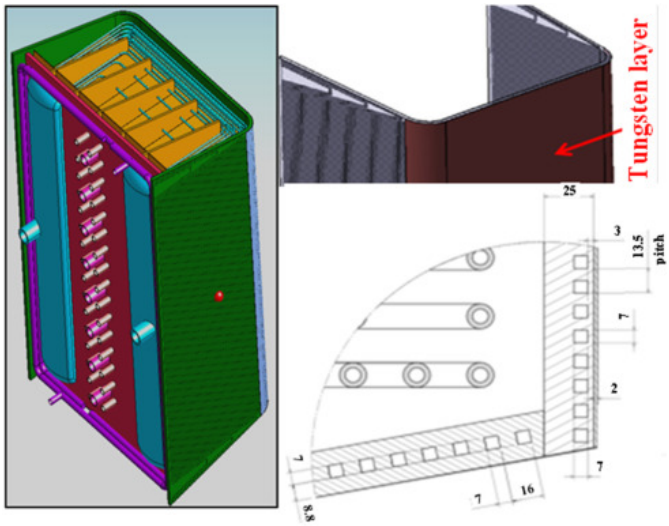

Figure 1.5: Layout of a First Wall module of DEMO reactor[22]

1.2 Aim of the work

The objective of this thesis work is to perform a 2D numerical analysis on PFCs exposed to RAE generated during disruption in DEMO fusion reactor, aimed at forecasting the damages, by means of a FEM solver.
Similar analysis has already been conduced for ITER, where the configuration of the components is slightly different as well as the forecasted energy loads. [23]
Differently from the thermal analyses of DEMO PFCs done until now, for normal operating conditions of the plasma, in which a superficial heat source is considered, in this work a volumetric heat souce is used, computed by ENEA by means of a Monte Carlo code FLUKA. The use of this tool allows to obtain a more accurate evaluation of the loads, since the the volumetric distribution of the energy released by the electrons penetrating in the mediums has been computed.
The thesis is structured in three parts.
In the first part, the set-up of the model used for the analysis is described. The first two sections include the description of the analysed geometries, with the choice of the computational domains and their discretization.

The third section includes an overview of the Monte Carlo analysis, with the results used to obtain the heat sources used as input for the model.
The boundary conditions, together with the correlation implemented are described in the fifth section.
The sixth section lists the material properties of both solid and fluid regions and explains how they have been implemented in the solver. The last includes the description of the initial condition used for each analysed configurations.
In the second part there is an overview of the results of the analysis (temperature patterns and evolutions) for each configurations.
All the results are then discussed in the last part of the thesis, with the conclusions of the work and the proposals for future developments.

Chapter 2

Numerical model

The numerical analysis has been conduced on a FE solver: Freefem++. [24]
The model built for the analysis is based on the 2D transient heat conduction equation with volumetric heat source

$$\frac{\partial T}{\partial t} = \alpha \nabla^2 T + \frac{\dot{q}'''}{\rho c_p}$$

where α is the thermal diffusivity equal to $\alpha = \frac{k}{\rho c_p}$.
The analysed domains, illustrated in section 2.1.3, have been properly discretized (see section 2.2) and, in order to allow the solution of the problem through the FE method, a finite element space of piecewise linear functions V_h has been defined on the analysed domain T_h. The variational form of the equation to be solved is

$$\int_{T_h} k \nabla T^{n+1} \nabla v + \int_{T_h} \rho c_p \frac{T^{n+1} - T^n}{\partial t} v - \int_{T_h} \dot{q}''' v = 0$$

where v is the so called test function defined in the FE space for the solution of the equation.
The approximation used to discretize the time is the implicit Backward Euler one. The choice of the time scheme used is due to its unconditional stability with a local truncation error of order one in time.
The time step used for the discretization has been chosen by means of a time convergence study discussed in section A.2.
In this chapter all the elements characterizing the model are illustrated together with the assumptions done in the set-up phase.

2.1 Computational domains for the thermal analysis

The energy profiles, used as input for the computation of the temperature patterns, have been computed by a Monte Carlo code FLUKA (illustrated in section 2.3.1), as mentioned in section 1.2.
Starting from the geometrical models used for the FLUKA code, for which energy deposition profiles have been produced, the computational domains of divertor element and FW have been simplified, in order to reduce the computational cost.

2.1.1 Divertor geometry

In the Monte Carlo analysis, the geometrical model consists of a 3-D layered structure with the X-, Y- and Z-axis oriented along the toroidal, the poloidal and the radial direction, respectively. The divertor element considered for the analysis has been divided into 22 identical modules, centered on the cooling tubes, with a toroidal length of 50 *cm* and a poloidal width of 2 *cm*. The cooling channels are arranged along a radial-poloidal path.
Figure 2.1 shows a zoom of a section of the divertor element described above. The element has a radial extension of 2.3 *cm*. The cooling tubes are composed by CuCrZr with a copper interlayer.

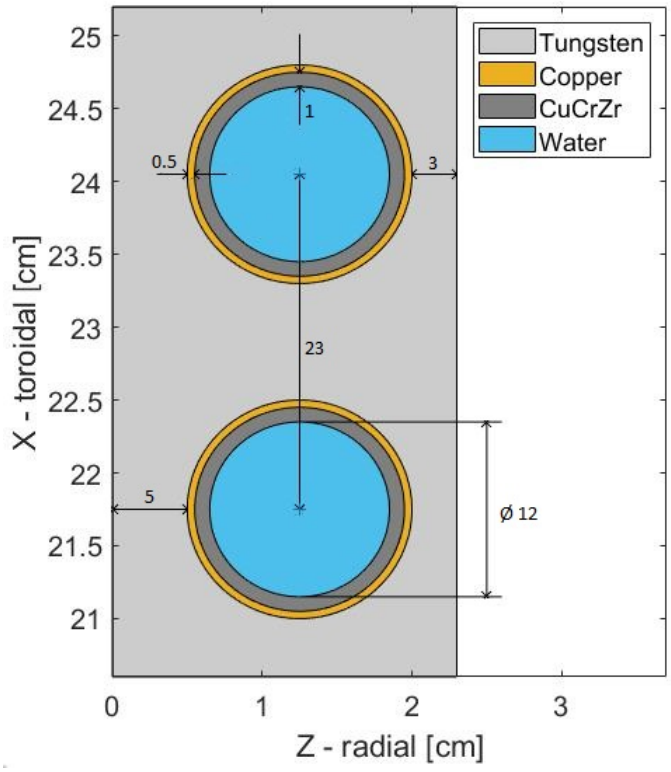

Figure 2.1: Materials and geometry of the divertor element (quotes in mm)

2.1.2 First wall geometry

In the Monte Carlo analysis, the geometrical model consists of a 3-D layered structure with the X-, Y- and Z-axis oriented along the toroidal, the poloidal and the radial direction, respectively. The segment of FW considered for the analysis has been divided into 36 identical modules, with a toroidal length of 50 cm and a poloidal width of 2 cm. The cooling channels have been arranged along a radial-poloidal path, as in the divertor structure.

Figure 2.2 shows a zoom of a section of the FW element described above. The element has a radial extension of 2.7 cm. The square cooling channels are drilled in the EUROFER region. The W armour has a thickness of 2 mm.

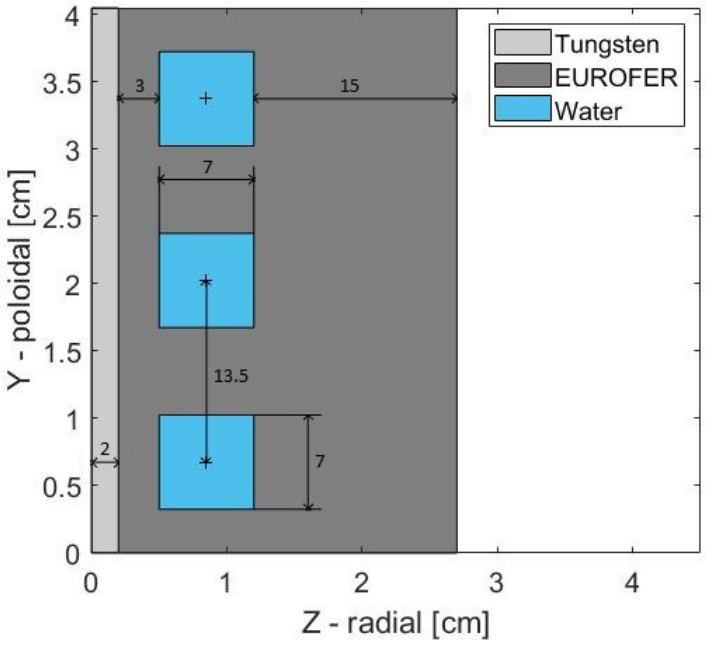

Figure 2.2: Materials and geometry of the FW element (quotes in mm)

2.1.3 Domains

The computational domain of both analysed components are shown in figure 2.3.

The divertor domain is located in a radial-toroidal plane in the central part of the geometry used for the Monte Carlo analysis, since the energy density is higher (see figure 2.5). Thanks to the symmetry of the geometry it has been possible to simplify the domain, considering only half module without the coolant region, since the energy deposited in the fluid is negligible with respect to the one deposited in the solid region (see figure 2.5) and thanks to the high Reynolds number (see section 2.5.2).

The FW domain is located in a radial-poloidal plane, differently from what is shown in section 2.1.2, since the arrangement used for the cooling channels for the Monte Carlo analysis was misinterpreted.

The pressurized water temperature in the channel of the FW changes, just like its mass flow rate, with the poloidal position of the element. In order to analyse the most critical condition, the domain is located in the highest region of the wall, where the coolant temperatures are higher and its mass flow rate is lower. As

the divertor domain, the FW one has been simplified thanks to symmetry of the geometry, considering only half module without the coolant region, since the energy deposited in the fluid is negligible with respect to the one deposited in the solid region (see figure 2.6) and thanks to the high Reynolds number (see section 2.5.2).

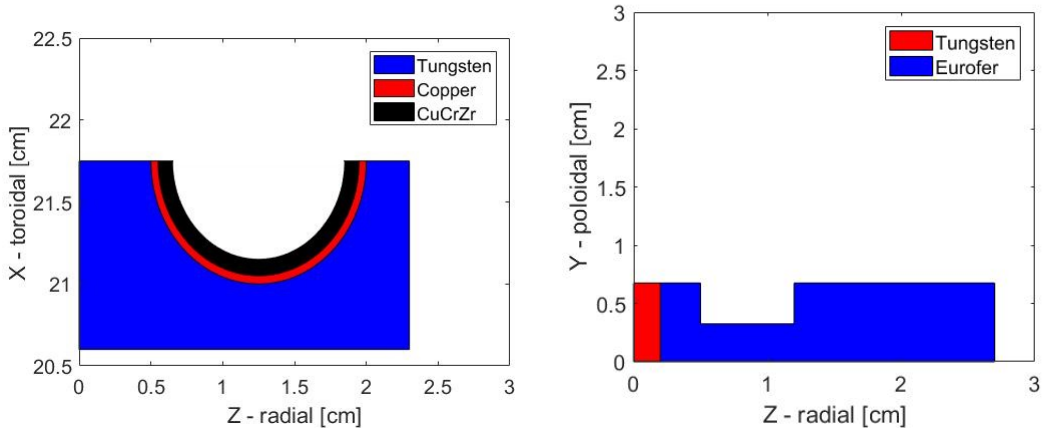

(a) (b)

Figure 2.3: Computational domains: (a) divertor and (b) First Wall, respectively

2.2 Mesh

The computational domain is discretized in Freefem++, using the command `buildmesh` to generate a 2D triangular unstructured mesh.

In order to obtain a uniform mesh, for a more accurate interpolation of the data computed in the Monte Carlo analysis (section 2.3.1), the borders are discretized with a number of points proportional to the one used to discretize the shortest edge.

Figure 2.4 shows an example of mesh for both divertor and FW domains. The grids used are much more refined than the ones shown in the figure.

The mesh has been chosen after a space convergence study illustrated in appendix A.1.

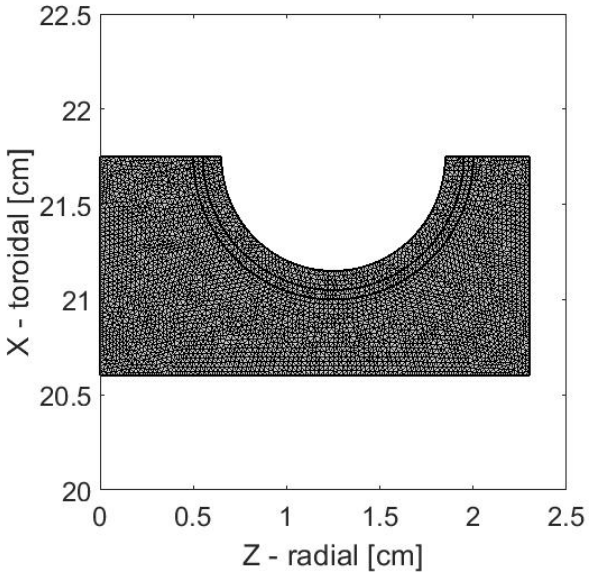

(a) *Divertor*

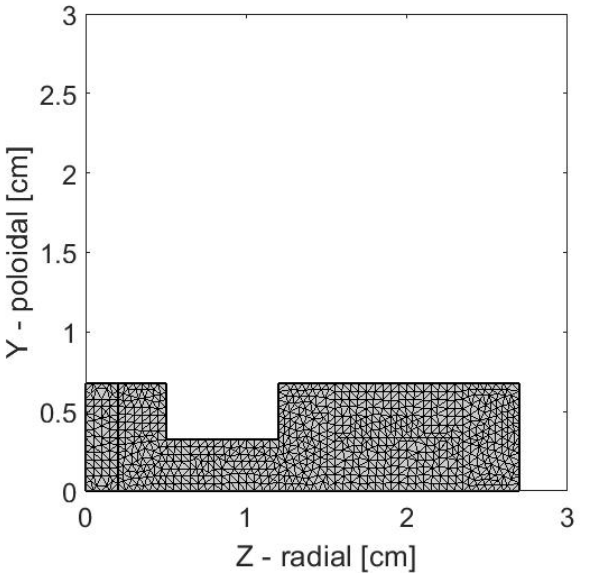

(b) *First Wall*

Figure 2.4: Mesh

Table 2.1 lists all the characteristics of the grids used in the analysis.

Configuration	Average characteristic length $[m]$	Number of elements
Divertor - 1°	$2.62e-05$	262118
Divertor - 10°	$3.39e-05$	180218
FW - 1°	$3.05e-05$	168964
FW - 10°	$3.05e-05$	168964

Table 2.1: Mesh characteristics

2.3 RAE heat load

The profile of the energy deposited by runaway electrons has been computed by means of the Monte Carlo code FLUKA. [25] [26]
The output of the code (shown in figures 2.5 and 2.6) has been normalized in order to obtain the heat source to be implemented in the model (section 2.3.2).

2.3.1 FLUKA code

FLUKA is a multi-particle Monte Carlo code, suitable to deal with particle and radiation transport problems. This code is able to give an accurate description of the most important electron-photon interactions, reproducing correlations as far as possible and avoiding unnecessary approximations.
The range of energies, that can be covered from the code, goes from few eV to thousands of TeV. For the specific problem of runaway electrons in DEMO, for both electrons and photons, the minimum threshold energy for production and transport is set to 100 keV.
The RAE beam energy has been considered as uniform and the single incident electron energy equal to 20 MeV. Gamma interactions with nuclei are switched off in FLUKA for this problem, since the contribution of the photonuclear reactions induced by gamma is negligible [27].
Two different incidence angles of the RAE beam have been considered for both the analysed components: 1° and 10°.

Energy deposition maps

The energy deposition in the code is scored both component by component (armour, heat sink, tube wall, cooling fluid in each module), to verify the energy balance fulfilling, and with geometry binning option, by subdividing the geometry into a spatial grid based on Cartesian axes. For both components, two different binning options have been used:

- a low resolution binning covering the full geometry (2 *cm* poloidal width and 50 *cm* toroidal length)
- a high resolution binning for the central part of the geometry (2 *cm* poloidal width and 8 *cm* toroidal length, centred at the X coordinate 20 *cm*)

In the table 2.2 the bin dimensions of both binning options are listed.

	X-toroidal [cm]	Y-poloidal [cm]	Z-radial [cm]
Low resolution	0.2	2	0.2
High resolution	0.025	2	0.025

Table 2.2: Binning options for Monte Carlo analysis

The maps of volumetric energy deposition of both divertor element and FW element are shown in figures 2.5 and 2.6. These profiles generated per single electron, need to be normalized on the total energy deposited on the components by the runaway beam, in order to be used for the computation of the temperature patterns.

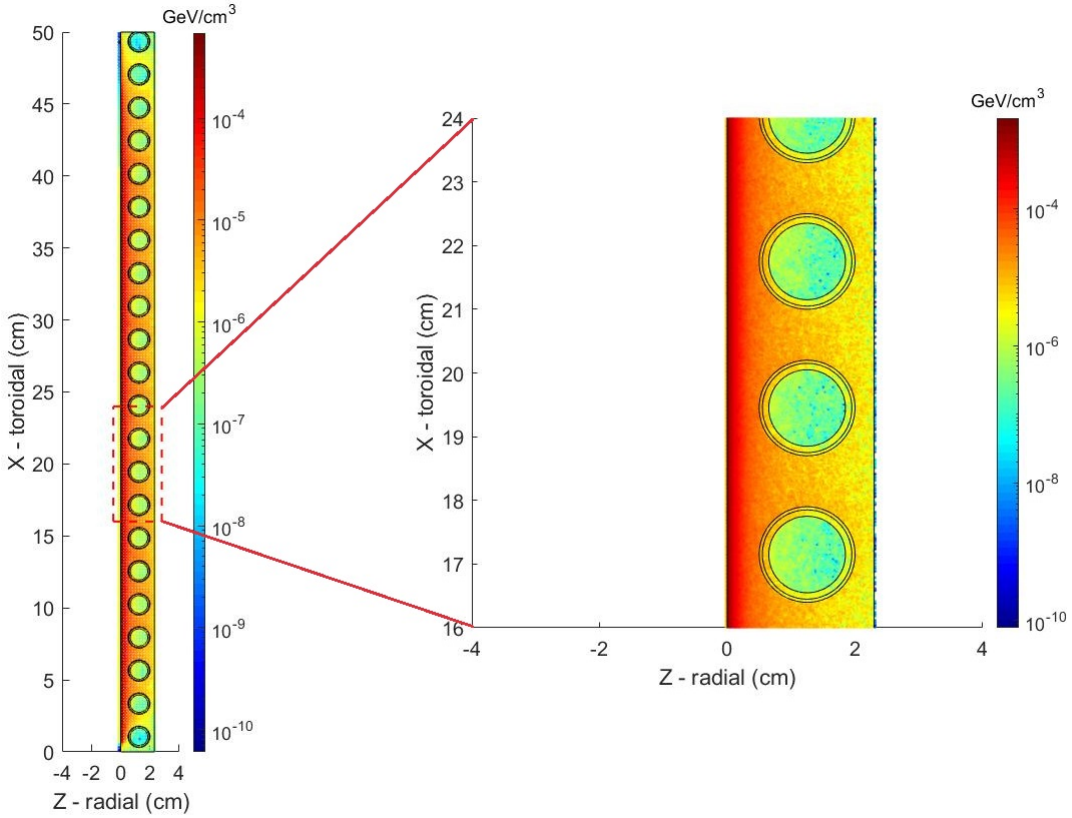

Figure 2.5: Volumetric heat deposition $[GeV/cm^3]$ in the divertor for a 1° RAE incidence angle

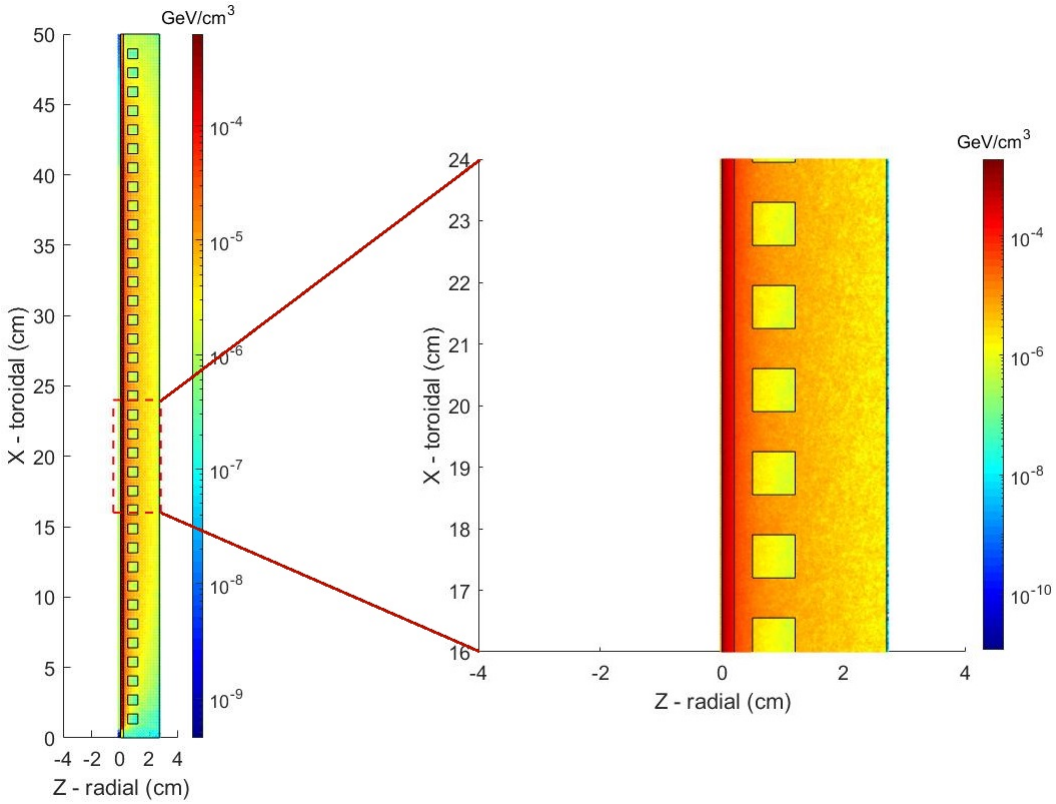

Figure 2.6: Volumetric heat deposition $[GeV/cm^3]$ in the FW for a 1° RAE incidence angle

2.3.2 Volumetric heat source for thermal analysis

As explained in section 1.1, runaway electrons are generated during disruptions at high current. There are several mechanisms and sources which affects the runaway generation, that can be mitigated injecting impurities in the plasma such as pure Ar or Ne.

Table 2.3 summarizes the ranges of runaway energy and runaway current for each impurity.

	Ar	Ne
Runaway current [MA]	$13 \div 16$	$15 \div 17$
Runaway beam energy [MJ]	$50 \div 60$	$40 \div 50$

Table 2.3: Runaway beam energy and current [17]

The highest runaway current and beam energy are predicted for the longest current quenches (100 ms).

The value of the beam energy chosen for the thermal analysis is the one associated to the worst scenario:

$$E_{beam} = 60\ MJ$$

The RAE beam diameter is equal to at least half of the plasma diameter before RAE production, so the incident area of the beam on the PFCs is more extended than the surface analysed in Monte Carlo analysis (2 cm x 50 cm). In order to take into account this difference, the value of the beam energy has properly re-scaled with a factor equal to 10^{-2}.

The beam duration (energy deposition time) has been considered same order of magnitude of the current quench time

$$t_{dep} = 200\ ms$$

and the power deposition has been assumed as constant with time.

Once these two values have been fixed, the energy profiles, computed by means of FLUKA code, have been properly normalized integrating the results of the Monte Carlo analysis on the entire considered geometry:

$$E_{beam} = \sum_{i=1}^{n}\sum_{j=1}^{m} \gamma e_{ij} dv$$

being n the number of bins along X-direction and m the number of bins along Y-direction, e_{ij} the energy deposited per unit of volume by a single electron in the bin ij and γ the normalization factor.

Figures 2.7 and 2.8 show the normalized power density maps, used for the analysis, for both the beam incidence angles taken into account in the Monte Carlo analysis.

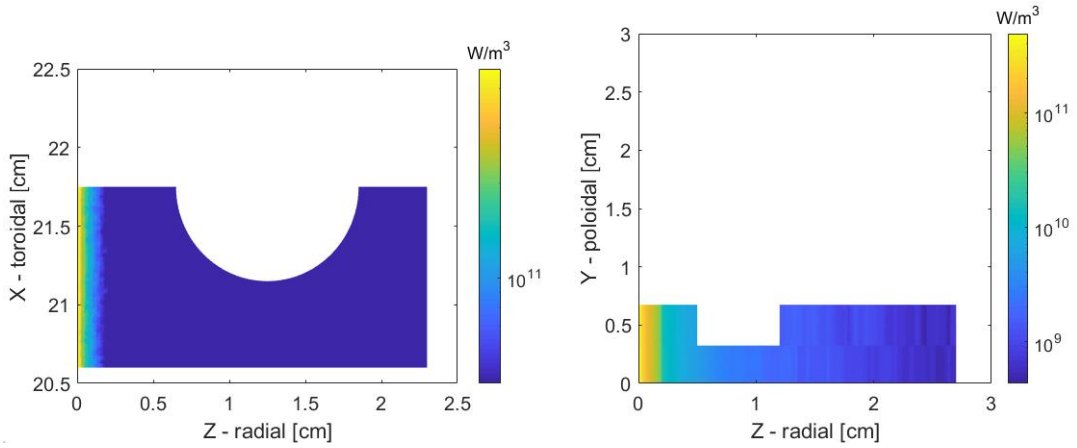

Figure 2.7: Power density maps for 1° incidence angle: (a) divertor and (b) First Wall, respectively

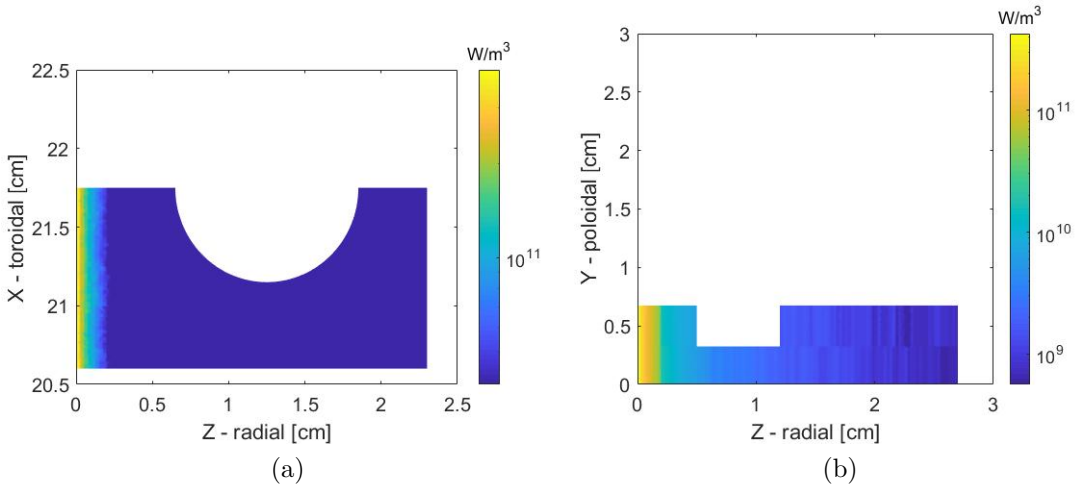

Figure 2.8: Power density maps for 10° incidence angle: (a) divertor and (b) First Wall, respectively

In table 2.4 the data of the maximum power density and the ones of power deposited on the analysed domain are summarised. The energy deposited in the element is the same for each incidence angle, but in the 1° configuration the maximum

power density is higher, since the deposition is concentrated on the inner surface of W, while in the 10° configuration the beam permeates more deeply in the PFC. The tungsten is expected to reach faster its melting point in 1° configuration, while in 10° configuration the core will reach higher temperatures.

Configuration	Maximum power density $[kW/cm^3]$	Power deposited $[kW]$
Divertor - 1°	461	86
Divertor - 10°	396	85
FW - 1°	486	51
FW - 10°	423	50

Table 2.4: Heat source characteristics

In the analysis two different scenarios have been considered, connected to the moment when disruption occurs:

- beam generated during the plasma start-up: the component is at a constant temperature equal to the one of the coolant
- beam generated when the plasma is at steady state operation: the initial temperature distribution depends from the heat load in this condition

For the divertor element, both the scenarios have been analysed, assuming as heat load in normal operating conditions, the target value of 10 MJ/m^2. For the FW element, the analysis has been carried on only for the first scenario.

2.4 Boundary conditions

The solution of the problem (shown at the beginning of this chapter) must satisfy constraints called boundary conditions.
For the analysed problem, in both component, only two types of boundary conditions have been used:

- Neuman homogeneous BC: the derivative of the solution normal to the boundary is null. This means no heat is exchanged on that boundary. This conditions has been fixed on the symmetry boundaries and on the external wall, in order to obtain a more conservative solution.

- Neuman non homogeneous BC: the derivative of the solution normal to the boundary, multiplied by the thermal conductivity, is equal to the value of the heat flux exchanged. This condition has been fixed on the convective pipe wall (cb), where the component is cooled by water, and on the radiative inner wall (rb), where the hot surface hit by the RAE beam will transfer heat by irradiation towards the remaining part of the FW

The boundaries are highlighted in figure 2.9.

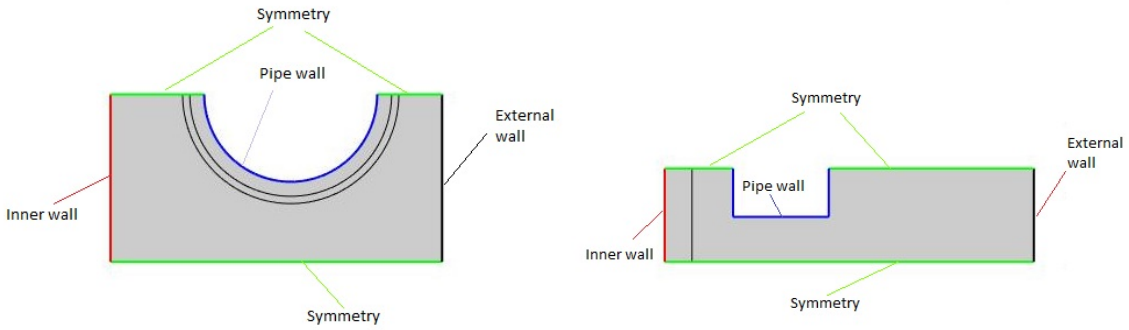

(a) *Divertor* (b) *First Wall*

Figure 2.9: Boundaries

The equation solved on Freefem++, including the boundary conditions is

$$\int_{T_h} k\nabla T^{n+1}\nabla v + \int_{T_h} \rho c_p \frac{T^{n+1}-T^n}{\partial t} v - \int_{T_h} \dot{q}''' v + \int_{cb} (\dot{q}_{bw} + \dot{q}_{conv}) v + \int_{rb} \dot{q}_{rad} v = 0$$

The code used to implement the equation on Freefem++ is

```
problem transient(Tnew,v)=int2d(Th)(kk*(dx(Tnew)*dx(v)
                                        +dy(Tnew)*dy(v)))
```

```
+int2d(Th)(rho*cp*Tnew*v/dt)
-int2d(Th)(rho*cp*TT*v/dt)
-int2d(Th)(qq*v)
+int1d(Th,903)(qrad*v)
 +int1d(Th,101)(qwall*v);
```

where `qq` is the volumetric heat source, `qrad` is the radiative heat flux released on boundary `903`, `qwall` is the convective heat flux exchanged on boundary `101`, `Tnew` is the temperature at time step $n+1$ and `TT` is the temperature at time step n.

2.4.1 Convective heat transfer correlations

The convective heat flux is generally computed as

$$\dot{q}_{conv} = A(T_{wall} - T_{bulk})$$

The correlation used in the model to compute the heat transfer coefficient (HTC) between the inner wall and the heat sink, differs according to the analysed regime:

1. Sieder-Tate correlation for the forced convection regime ($T < T_{sat}$) [28]
2. Rohsenow correlation for the subcooled boiling regime ($T >= T_{sat}$) [29]

Sieder-Tate correlation, differently from the most used Dittus-Boelter one, allows to compute a local value of the heat transfer coefficient that is temperature dependent. The correlation for the Nusselt number Nu is

$$Nu = 0.027 Re^{0.8} Pr^{\frac{1}{3}} \left(\frac{\mu}{\mu_s}\right)^{0.14}$$

where Re is the Reynolds number, equal to $Re = \frac{\dot{m} \cdot D_H}{\mu \cdot A}$, $\dot{m}$ is the mass flow rate, μ is the viscosity of water at T_{bulk}, D_H is the hydraulic diameter, A is the heat exchange area, Pr is the Prandtl number, equal to $Pr = \frac{c_p \cdot \mu}{k_w}$, c_p is the specific heat of water a T_{bulk}, k_w is the thermal conductivity of water at T_{bulk} and μ_s is the viscosity of water at T_{wall}.
The heat transfer coefficient is then computed as $h = \frac{k_w}{D_H} Nu$
The figure 2.10 shows the heat transfer coefficient in the forced convection regime.

By means of the software Matlab, an interpolating function has been computed for each components (due to the different properties of the coolant) and then implemented in the model on Freefem++.

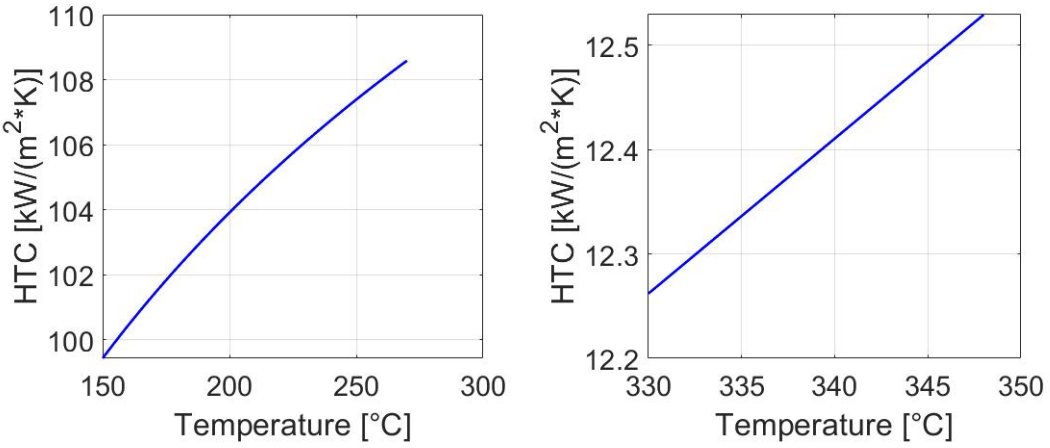

(a) *Divertor* (b) *First Wall*

Figure 2.10: Heat transfer coefficient (HTC) in forced convection regime

Rohsenow correlation simulates the fluid as single-phase and is used to compute directly the heat flux exchanged at the wall in boiling regime, to be sum to the heat flux exchanged in forced convection regime at saturation temperature, following the superposition principle

$$\dot{q}_{bw} = \mu_l h_{lat} \sqrt{\frac{g(\rho_l - \rho_v)}{\sigma}} \left(\frac{C_{pl}(T_{wall} - T_{sat})}{C_{qw} h_{lat} Pr^{np}} \right)^{3.03}$$

where μ_l is the liquid dynamic viscosity at T_{sat}, h_{lat} is the latent heat of vaporization, g is the gravitational acceleration, ρ_l and ρ_v are the liquid and the vapour density at T_{sat}, respectively, σ is the surface tension at T_{sat}, C_{pl} is the liquid heat capacity at T_{sat}, C_{qw} is an empirical coefficient depending on the solid-liquid interface conditions assumed equal to 0.0147, np is the exponent of the Prandtl number equal to 1 [30]. For the implementation of this correlation in the model, a damping function is looked for to avoid the instabilities in the simulation. These instabilities are due

to the incorrect computation of a convective power exchanged, higher than the one deposited in the analysed domain. In order to reduce this phenomenon (or delete it), the correlation has been implemented in a different way

$$\dot{q}_{bw} = \mu_l h_{lat} \sqrt{\frac{g(\rho_l - \rho_v)}{\sigma}} \left(\frac{C_{pl}(T_{gm} - T_{sat})}{C_{qw} h_{lat} Pr^{np}} \right)^{3.03}$$

where T_{gm} is the wall temperature geometric mean between the two previous iterations of the model. [31]

2.4.2 Radiative heat transfer correlation

The formula used to compute the radiative heat flux released by the inner surface of the PFC is the Stefan-Boltzmann law, valid for blackbodies.
A blackbody is defined as a perfect absorbing and emitting surface.
The correlation states that the emissive power of a blackbody is proportional to the fourth power of its surface temperature

$$q = \sigma T^4$$

where σ is the Stefan-Boltzmann constant equal to $5.670 \cdot 10^{-8}\ W/(m^2 \cdot K^4)$.
Being a blackbody an ideal condition, the Stefan-Boltzmann law is modified introducing a factor called emissivity, defined as the ratio of the power emitted by a real surface and the power emitted by a blackbody at the same temperature.[32]
The heat flux emitted by the surface hit by runaway beam is computed as

$$\dot{q}_{rad} = \sigma \epsilon (T^4 - T_{m,FW}^4)$$

where the emissivity has been assumed $\epsilon = 0.4$ [33] for the tungsten and the average temperarture of the FW surface is assumed $T_{m,FW} = 550\ ^oC$ in normal operating condition of the plasma.

2.5 Material properties

2.5.1 Solid region

Figure 2.11 shows the thermal properties of W [34][35], Cu [36], CuCrZr [37] and EUROFER97 [38] used for the analysis. For the temperature dependent properties,

suitable equations have been computed, starting from literature databases. The constant properties are listed in the graphs too.

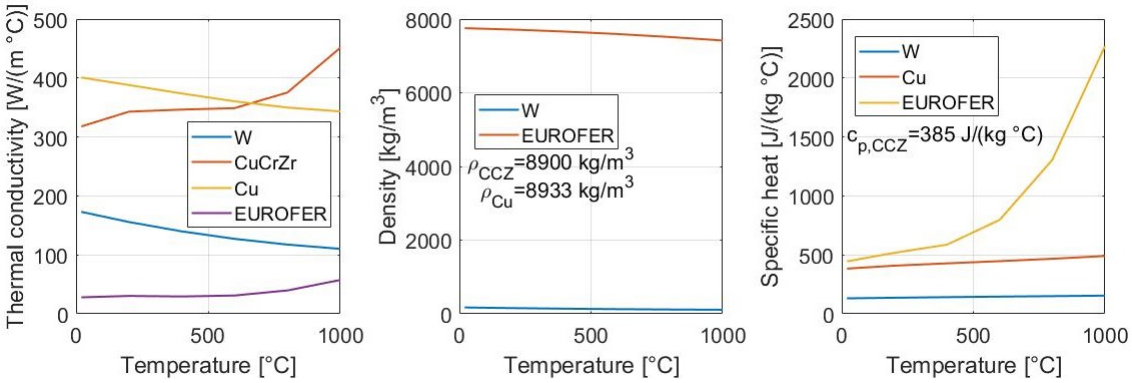

Figure 2.11: Material properties

Figure 2.12 shows the thermal properties of W in liquid phase. Since the beam deposits the main fraction of energy in the first 2 mm of W, it is expected to reach its melting point, so suitable equations have been computed for W thermal properties in liquid phase too. The specific heat is constant and equal to $c_{p,W} = 279.81\ J/(kg \cdot K)$.

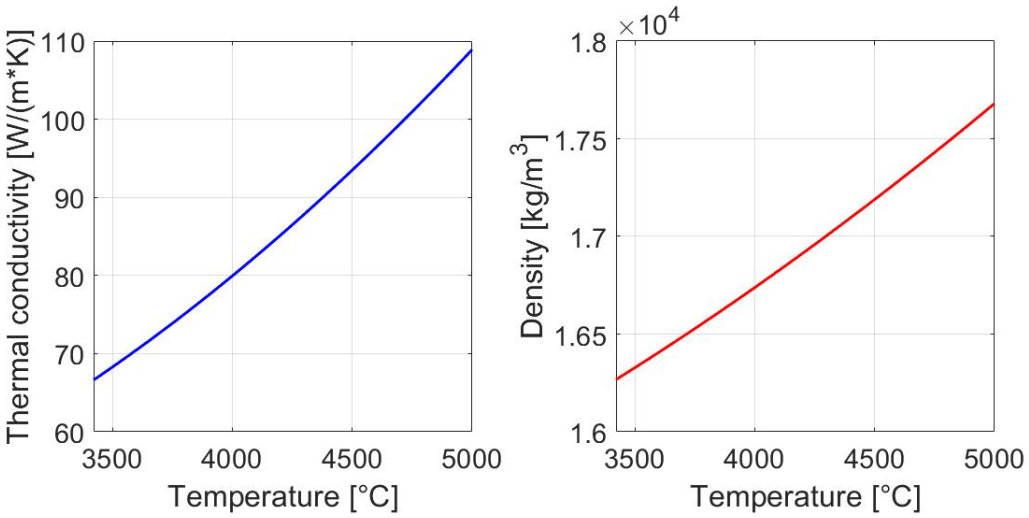

Figure 2.12: W properties in liquid phase

The melting points of each materials are listed in table 2.5 (for EUROFER97 the value has been assumed, due to the lack of data).

Material	T_{melt} $[°C]$
W	3421.85
Cu	1085
CuCrZr	1075
EUOFER97	1100

Table 2.5: Melting temperatures

The tungsten region will undergo the highest rise of temperature and it is expected to reach its melting point in both divertor and FW, since the highest fraction of energy is deposited in the first 2 mm of W, as shown in figures 2.7 and 2.8.
The melting of W has been analysed by means of the apparent heat capacity method. In this numerical fixed-grid method the phase-change is investigated in a defined temperature range between $T_{sol} = T_{melt} - \delta$ and $T_{liq} = T_{melt} + \delta$ (mushy zone), where δ has been assumed equal to 5 ^oC. The heat conduction equation is

then solved implementing for the specific heat of W a piecewise function as shown in figure 2.13, with the value in mushy zone computed as

$$c_{mz} = \frac{\Delta h_f}{T_{liq} - T_{sol}}$$

with the latent heat of fusion equal to $\Delta h_f = 52.3\ kJ/mol$.

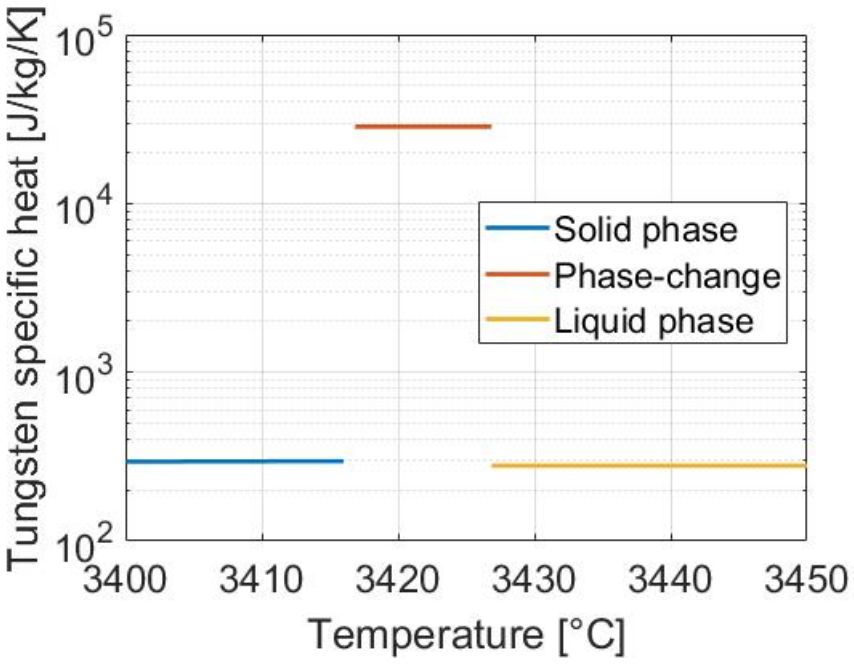

Figure 2.13: Specific heat of W during phase-change

The choice of a fixed grid method is a simplification done in order to avoid, in first approximation, the use of a movable boundary and the possibility of loss of material.
The boiling of W has been neglected, in first approximation, for the same reason. The thermal properties of the region exceeding the boiling temperature (equal to 5660 ^oC [39]) have been assumed as constant and equal to the ones at T_{boil} for the computation.

Since the thermal properties of the materials are temperature dependent, an iterative method should guarantee a better evaluation of the temperature T at the

step $n+1$. In order to reduce the computational cost, the frozen coefficient method has been adopted, computing the properties as function of T^n and avoiding the use of an iterative method.

2.5.2 Cooling fluid

The cooling system of both the PFCs analysed, uses pressurized water as fluid. In table 2.6, the data used for the analysis are summarized. Due to the high Reynolds number, in order to simplify the computation, the water has been considered at a constant temperature equal to T_{bulk}. This simplification allows not considering the fluid region, but suitable correlations have to be used to take into account the high temperature drops that can be reached at the solid-liquid interface (see section 2.4.1), which can cause the boiling of water on the contact surface.

	FW	Divertor
$P\ [MPa]$	15.5	5.5
$T_{sat}\ [^oC]$ [40]	344.8	270
$v\ [m/s]$	1	16
$T_{bulk}\ [^oC]$	340.2	156

Table 2.6: Coolant data

T_{bulk} has been chosen, in order to analyse the worst case, for both component, assuming that the runaway beam could hit any zone in the vessel with the same probability. For the divertor element, the temperature considered is the one at the outlet section of the cooling channel. For the FW element, the temperature considered is the maximum one that can be reached in the cooling channels, located in the highest region of the wall.

2.6 Initial condition

The initial condition of the problem depends on the analysed scenario (see section 2.3.2):

- In case of disruption during the start-up phase of the plasma, the reactor would be still cold, so the temperature is assumed as constant and, for simplicity, equal to the one of the coolant (156 $°C$ for the divertor and 340.2 $°C$)
- In case of disruption occurring when the plasma is at normal operating condition (for divertor), the initial temperature pattern depends on the heat load, assumed equal to 10 $MJ/m2$. This profile is shown in figure 2.14

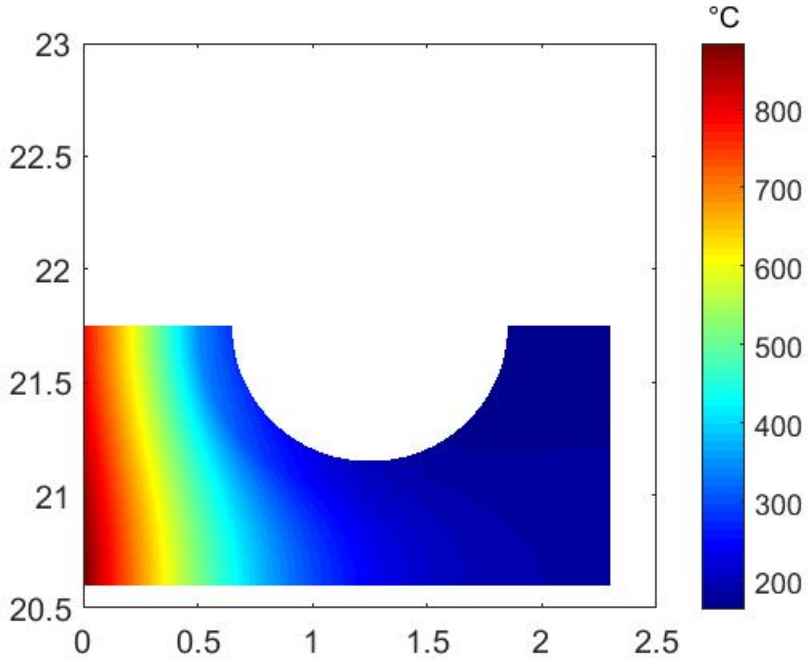

Figure 2.14: Temperature profile in normal operating conditions

The initial temperature profile can strongly affects the final solution, since the maximum temperature of W is higher of 800 $°C$ in normal operating conditions and the maximum temperature at the pipe wall is higher than T_{sat}.

Chapter 3

Results

In this section the main results of the numerical 2D analysis are shown and discussed. The main analysed results for each configuration are:

- maximum temperature evolution in each materials, in order to investigate whether the melting point is reached or not
- maximum temperature evolution at pipe wall, in order to study the behaviour of the cooling fluid
- final temperature distribution, in order to account the damages caused by RAE beam

3.1 Divertor - Scenario 1

The transient has been analysed for the entire deposition time (200 ms), starting from the constant initial temperature equal to 156 $°C$, a thickness of W region overcomes the melting point, while the temperature of the layers of cooling pipes remains always below the melting point of copper and CuCrZr for both configurations of beam incidence angle (figure 3.1).

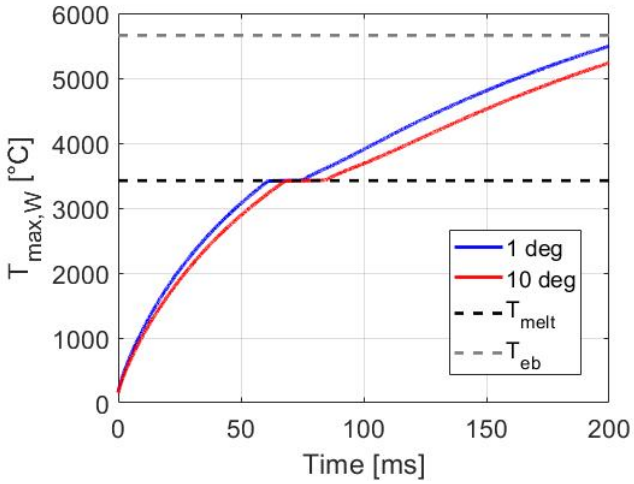

(a) *Temperature of W region*

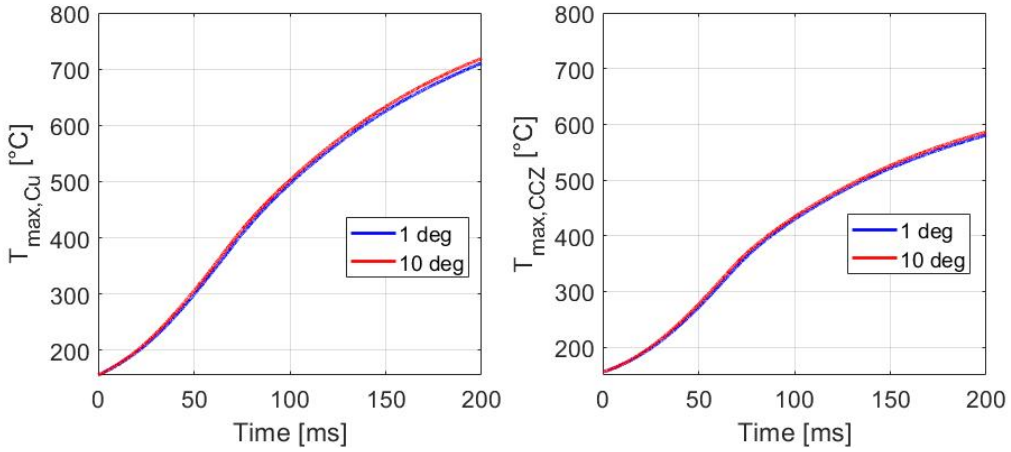

(b) *Temperature of pipe layers*

Figure 3.1: Maximum temperature evolution in scenario 1 for divertor component

The maximum temperature on the pipe wall overcomes the saturation temperature of the water at 5.5 MPa, so nucleate boiling is expected to form and the heat transfer coefficient is enhanced (figure 3.2). The temperature difference ΔT_{sat} is higher than 30 $°C$, so the convective heat flux might overcome the critical heat flux (CHF) and the surface of the pipe would be completely covered by a vapour blanket, which hinders the heat exchange. In figure 3.3 the temperature profile on the pipe wall is illustrated: since the area above the saturation temperature is lower

than 35% of the total exchange area, the analysis on CHF has been neglected and the correlations used for the heat transfer have been considered acceptable.

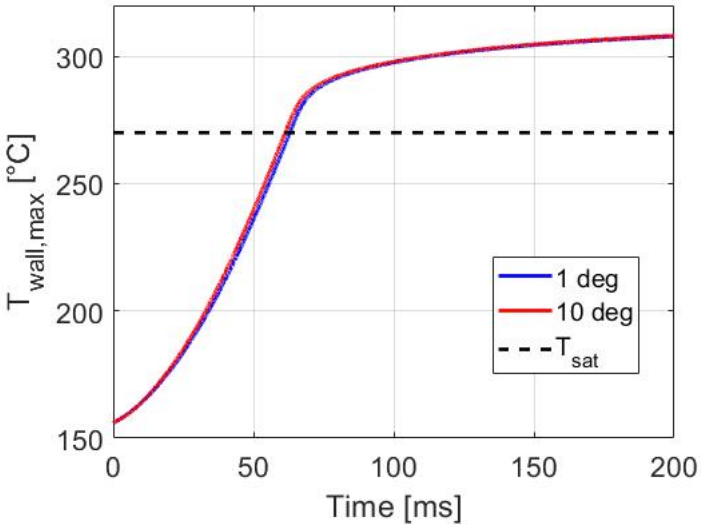

Figure 3.2: Maximum temperature evolution on pipe wall in scenario 1 for divertor component

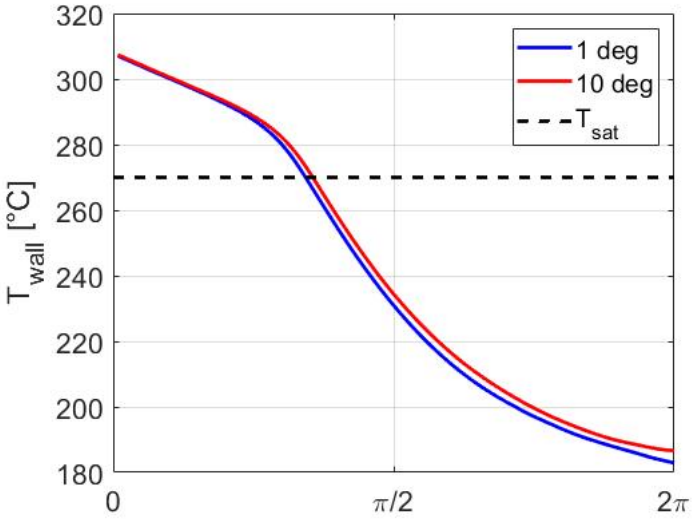

Figure 3.3: Temperature profile on pipe wall in scenario 1 for divertor component

Figures 3.4 and 3.5 show the final temperature patterns in both incidence angle configurations, for the first analysed scenario. The amount of melted W is shown in grey. In both cases the melted region corresponds to a thickness of 2 mm.

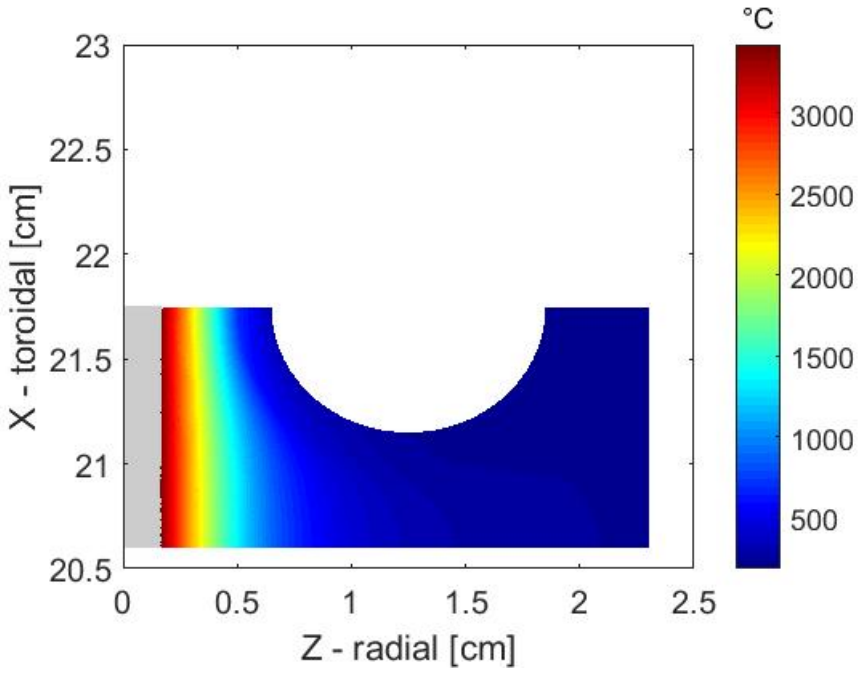

Figure 3.4: Final temperature pattern for a 1° incidence angle in scenario 1

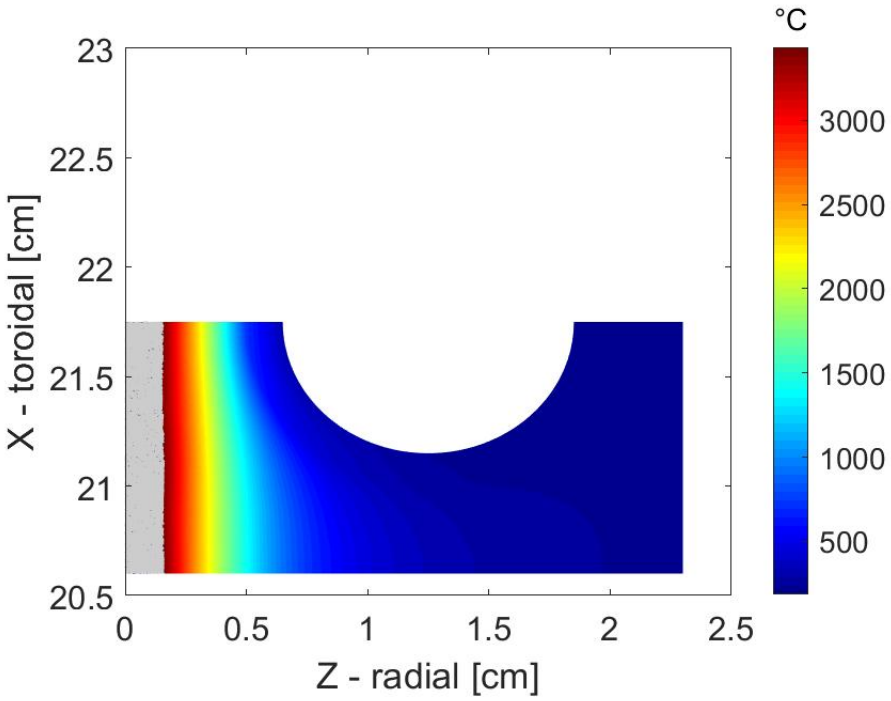

Figure 3.5: Final temperature pattern for a 10° incidence angle in scenario 1

For the 1° incidence angle configuration the transient has been analysed even after the deposition time, in the cooling phase, without the volumetric heat source, in order to highlight the behaviour of the divertor. The assumptions for this analysis are the same done for the previous analysis (no loss of material). Figure 3.6 shows the maximum temperature evolution in time of all the regions. While the maximum temperature of W strongly drops down at the beginning of the cooling phase, the temperature in the pipe layers has a little rise, due to the heat conduction from the hot zone of the component. The cooling phase is much slower than the heating one, but all the melted tungsten might solidify in a time interval lower than 0.5 s.

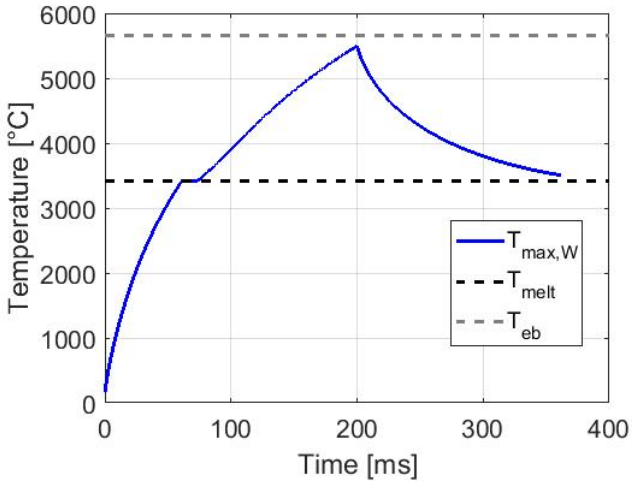

(a) *Temperature of W region*

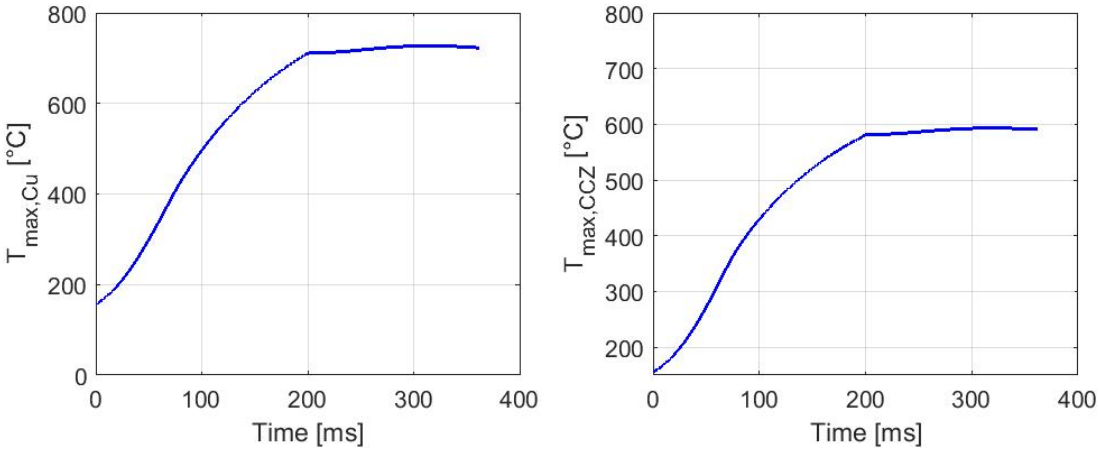

(b) *Temperature of pipe layers*

Figure 3.6: Maximum temperature evolution in cooling phase

3.2 Divertor - Scenario 2

The transient has been analysed for the entire deposition time (200 ms), starting from the initial temperature profile equal to the one in normal operating conditions, when the incident heat flux on the inner surface is equal to 10 MW/m^2 (see figure 2.14). A thickness of W region overcomes the melting point, while the temperature of the layers of cooling pipes remains always below the melting point of copper and CuCrZr for both configurations of beam incidence angle (figure 3.7). In the 1°

configuration the maximum temperature of W reaches the boiling point too.

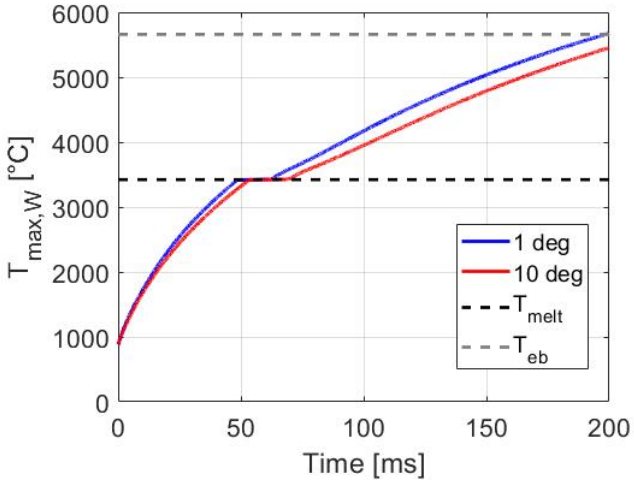

(a) *Temperature of W region*

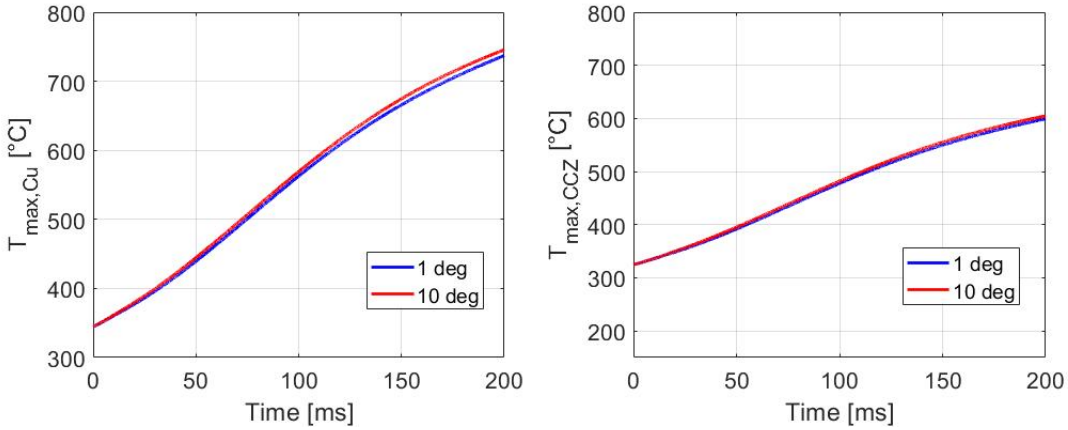

(b) *Temperature of pipe layers*

Figure 3.7: Maximum temperature evolution in scenario 2 for divertor component

The maximum temperature evolution on the pipe wall is shown in figure 3.8, while figure 3.9 illustrates the temperature profiles on the wall. As in the first scenario, the analysis on CHF has been neglected and the correlations used for the heat transfer have been considered acceptable.

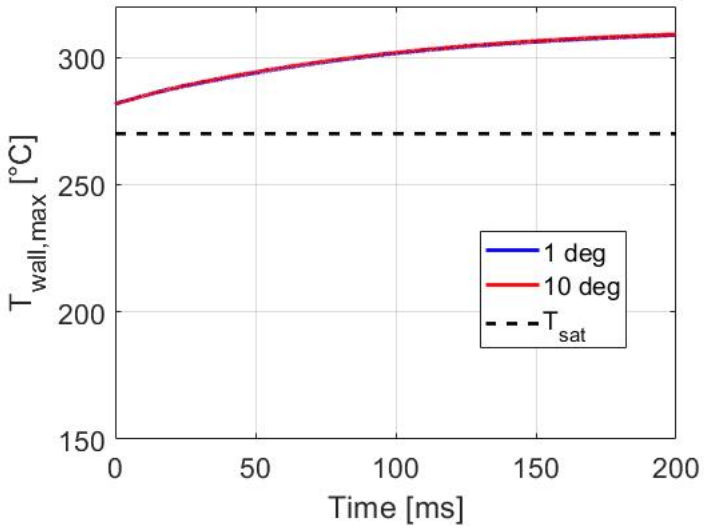

Figure 3.8: Maximum temperature evolution on pipe wall in scenario 2 for divertor component

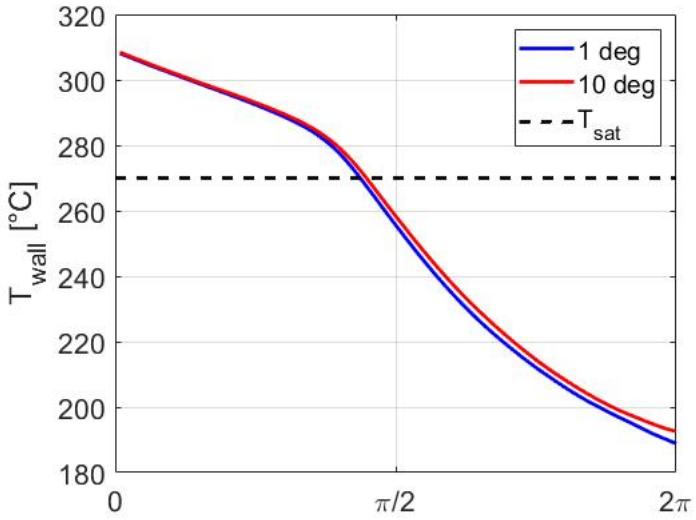

Figure 3.9: Temperature profile on pipe wall in scenario 2 for divertor component

Figures 3.10 and 3.11 show the final temperature patterns in both incidence angle configurations, for the first analysed scenario. The amount of melted W is shown in grey. In both cases the melted region corresponds to a thickness of 2 mm.

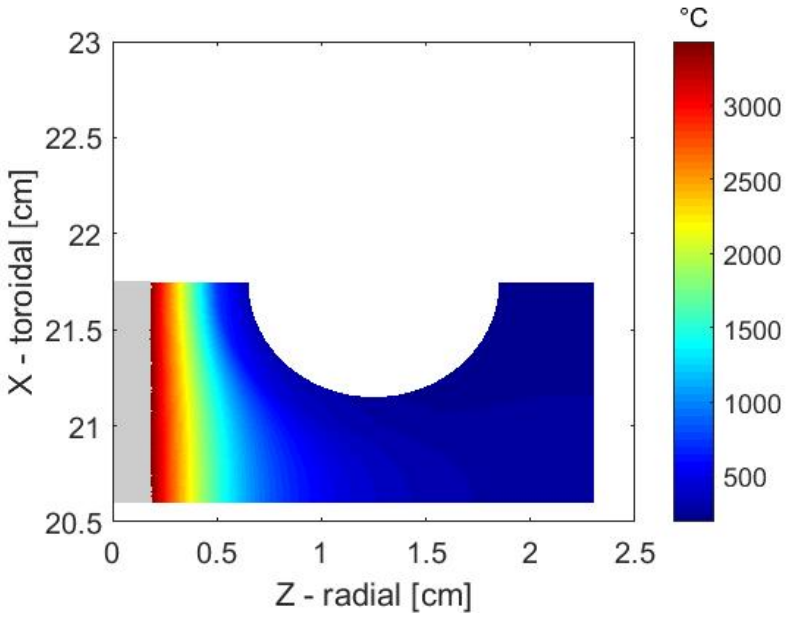

Figure 3.10: Final temperature pattern for a 1° incidence angle in scenario 2

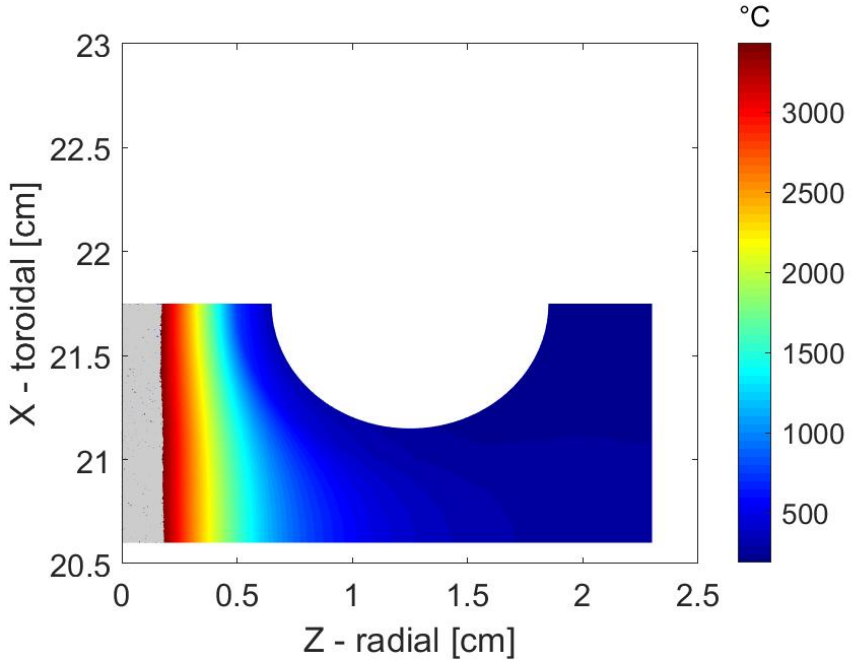

Figure 3.11: Final temperature pattern for a 10° incidence angle in scenario 2

As expected the second analysed scenario is more critical than the first, since the overall resulting temperature profiles for both the incidence angle configurations are higher.

3.3 First Wall

Differently from the divertor component case, the transient for FW has not been analysed for the whole deposition time, since a critical condition occurs before: the melting of the EUROFER region. The analysis has been carried on until the maximum temperature of EUROFER reaches a value close to its melting point (assumed equal to 1100 $°C$). Figure 3.12 shows the maximum temperature evolution of both W and EUROFER region. When the critical condition occurs, the tungsten region has not still reached its melting point.

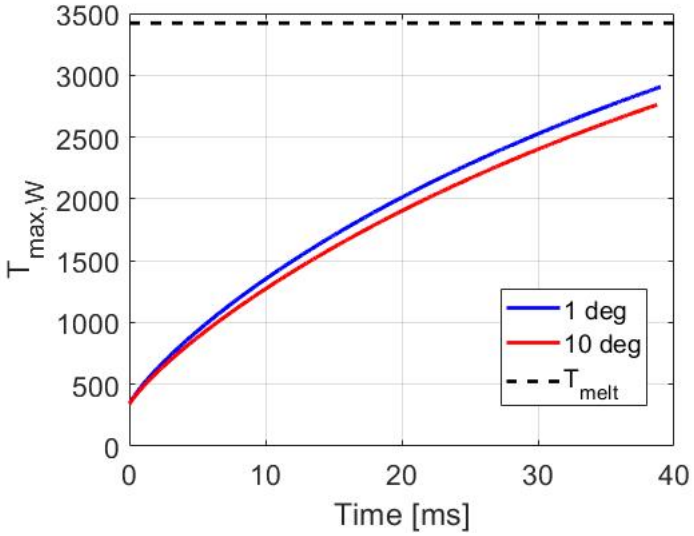

(a) *Temperature of W region*

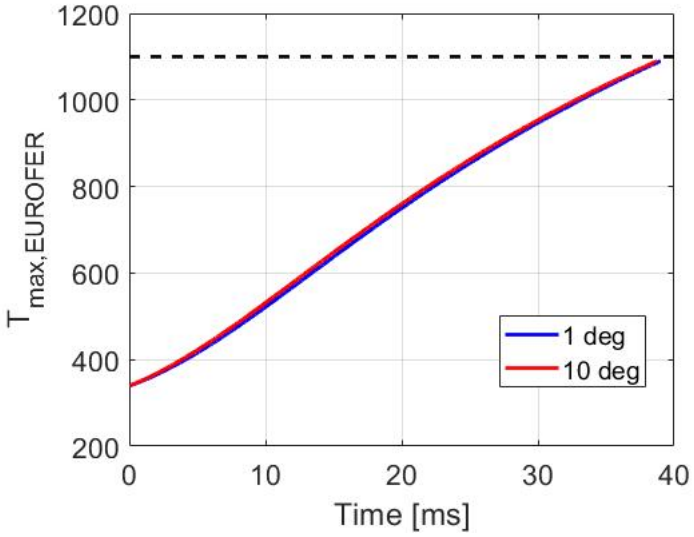

(b) *Temperature of EUROFER region*

Figure 3.12: Maximum temperature evolution for FW component

Figure 3.13 shows the temperature distribution near the inner wall of the FW component. This picture highlights that the temperature along the poloidal direction is quite uniform and the melting of the EUROFER should interest the entire contact surface with W.

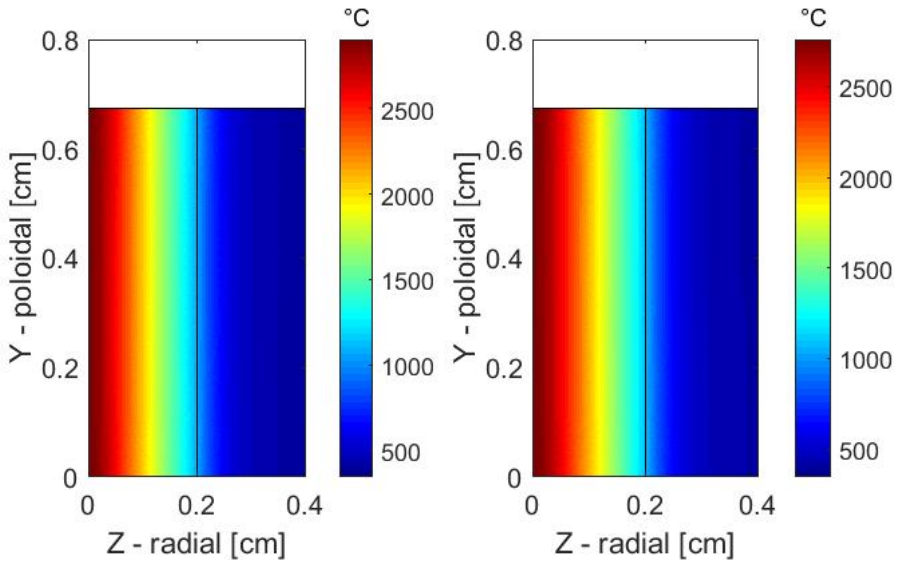

(a) 1° *incidence angle* (b) 10° *incidence angle*

Figure 3.13: Temperature distribution near the wall hit by RAE beam, in FW component

Chapter 4

Summary and conclusions

The purpose of this thesis work was to perform a thermal analysis on plasma facing components in DEMO fusion reactor (first wall of the blanket and divertor), hit by a runaway electron beam generated during disruptions in the plasma, in order to account the possible consequent damages.
The analysis has been carried on by means of a model described in the second part of the thesis, implemented on a FEM solver FreeFem++. The volumetric energy maps used as input for the heat conduction code have been computed by means of the Monte Carlo code FLUKA and have been provided by ENEA. Once fixed the energy carried by the runaway beam (properly re-scaled) and the deposition time, the temperature patterns have been computed.
The main results, shown in the third part of the thesis, highlight the presence of damages in both divertor and first wall.
For the first wall the critical condition of melting of EUROFER region is reached in almost 20% of deposition time and it is not further analysed, due to the lack of data of material properties (such as the real melting point, the thermal properties in liquid phase and the latent heat of fusion).
For the divertor component a melting of $\sim 2\ mm$ of W in all the analysed configurations is forecasted, with the possibility of boiling in one of the cases. The melting of the cooling tubes is not expected to occur, so catastrophic accidents such as LOCA would not happen.
This work can be the starting point to more accurate analyses aimed to properly

design PFCs able to withstand high energy pulses due to runaway electron events, without the occurrence of big damages. Among the improvements that the analysis could require, there are:

- Improvement the geometry assessment: accounting the presence of limiters in the plasma chamber and evaluating the correct incidence surface of the runaway beam
- Implementation of different models for the phase-change in the tungsten region (such as the use of a movable boundary), accounting the loss of material, due to evaporation or removal by electromagnetic forces
- Evaluation of the maximum energy load that components in the current state of art can withstand, avoiding any damage
- Evaluation of the temperature rise in the cooling fluid, in order to forecast the presence of extended film boiling that would affect the performances of the cooling system, moving to a fully 3D simulation

Appendix A

Convergence studies

A.1 Space convergence study

The analysis has been done for every analysed configuration (2 for divertor and 2 for FW, considering the 2 different incidence angles), comparing the average temperature and the maximum one after 1 ms of transient. The number of elements on each edge have been changed and the error, on both the analysed temperature, has been computed with respect to the results on the most refined grid, assumed to be the most correct ones.
Figures A.1 and A.2 show the computed errors. For each configuration the chosen mesh is able to guarantee a relative error lower than 0.1% on both T_{av} and T_{max}, which has been considered as reasonable in order to have reliable results and to not increase the computational cost too much.

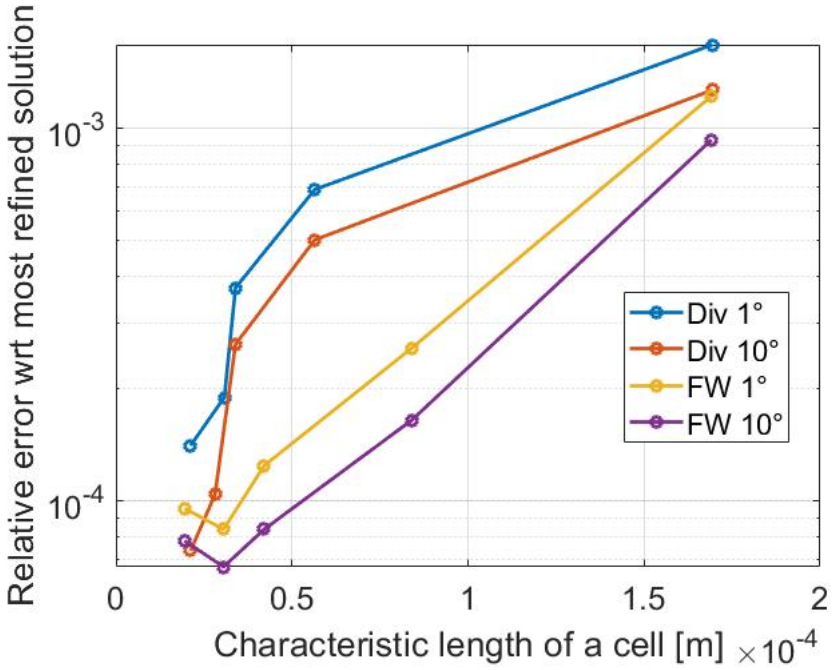

Figure A.1: Space convergence study on T_{av}

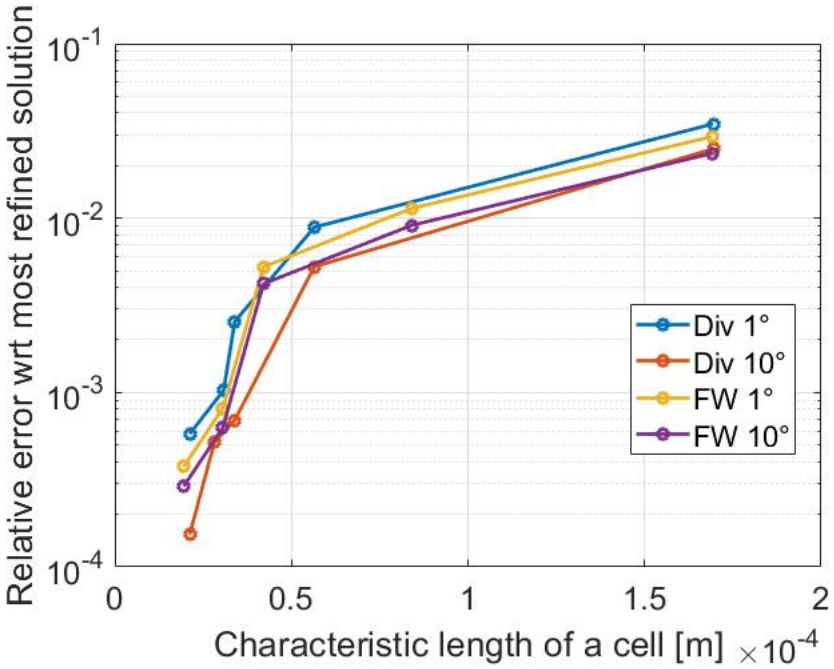

Figure A.2: Space convergence study on T_{max}

A.2 Time convergence study

The time convergence study has been done after the choice of the mesh. Just as in the space convergence study, the average temperature and the maximum one have been compared after 1 ms of transient.
Figures A.3 and A.4 show the computed errors. The time step chosen for all the configuration is $\Delta t = 0.01$ ms, that is able to guarantee a reasonable error, always lower than 0.5% on T_{max}, without increasing the computational cost too much.

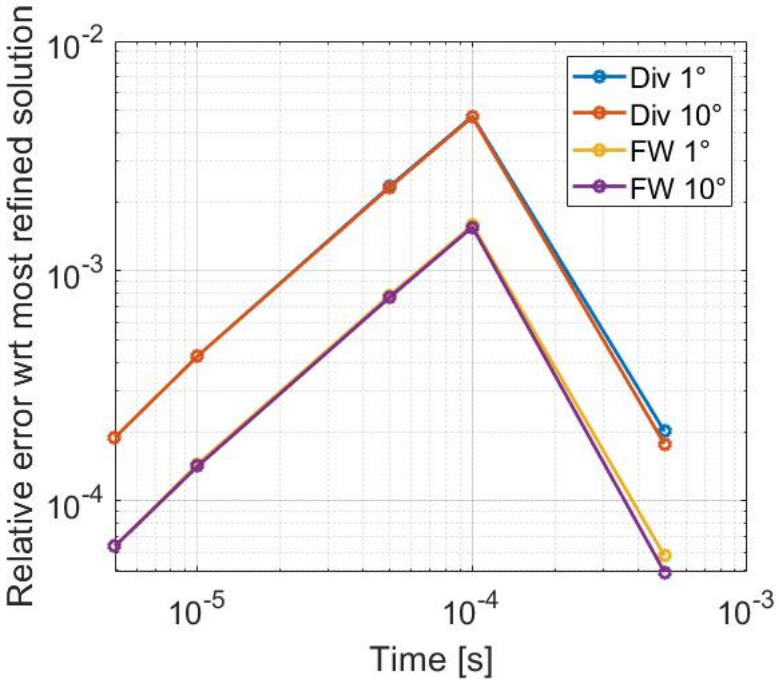

Figure A.3: Time convergence study on T_{av}

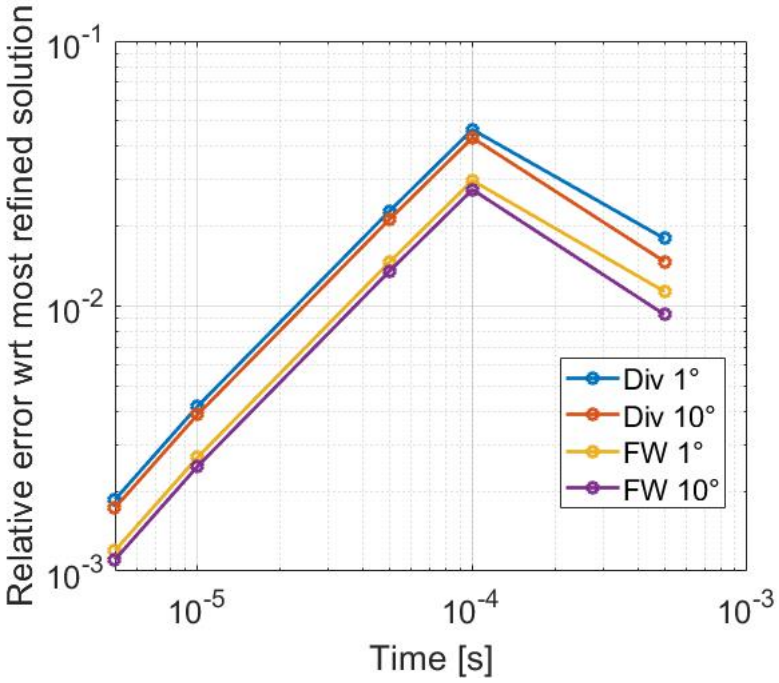

Figure A.4: Time convergence study on T_{max}

Bibliography

[1] www.iea.org (accessed on March 5th, 2019)

[2] G. McCracken, P. Stott, *Fusion, the Energy of the Universe*, Elsevier Academic Press, 2005

[3] J.K. Shultis, R.E. Fawm *Fundamentals of nuclear science and engineering*, CRC Press, 2002

[4] S.M. Weston, *Fusion An Introduction to Physics and Technology of Magnetic Confinement Fusion*, Physics Textbook, Wiley-VCH Verlag GmbH &Co., 2010

[5] http://www.fusione.enea.it/WHAT/index.html.en (accessed on March 4th, 2019)

[6] J.P. Friedberg, *Plasma Physics and Fusion Energy*, Cambridge University Press, 2007

[7] https://www.euro-fusion.org/news/detail/detail/News/tokamak-principle/ (accessed on May 13th, 2019)

[8] J. Wesson, *Tokamaks*, Oxford University Press, 2004

[9] https://rdreview.jaea.go.jp/review_en/2014/9_9.html (accessed on September 17th, 2019)

[10] https://www.iter.org (accessed on March 7th, 2019)

[11] https://www.euro-fusion.org/programme/demo/ (accessed on March 7th, 2019)

[12] L.V. Boccaccini, G. Aiello, J. Aubert, C. Bachmann, T. Barrett, A. Del Nevo, D. Demange, L. Forest, F. Hernandez, P. Norajitra, G. Porempovic, D. Rapisarda, P. Sardain, M. Utili, L. Vala, *Objectives and status of EUROfusion DEMO blanket studies*, Fusion Engineering and Design, Volumes 109–111, Part B, 2016, 1199-1206

[13] E. Martelli, F. Giannetti, G. Caruso, A. Tarallo, M. Polidori, L. Barucca, A. Del Nevo, *Study of EU DEMO WCLL breeding blanket and primary heat transfer system integration*, Fusion Engineering and Design, Volume 136, Part B, 2018, 828-833

[14] R.A. Pitts, X. Bonnin, F. Escourbiac, H. Frerichs, J.P. Gunn, T. Hirai, A.S. Kukushkin, E. Kaveeva, M.A. Miller, D. Moulton, V. Rozhansky, I. Senichenkov, E. Sytova, O. Schmitz, P.C. Stangeby, G. De Temmerman, I. Veselova, S. Wiesen, *Physics basis for the first ITER tungsten divertor*, Nuclear Materials and Energy, Volume 20, 2019

[15] `https://www.flickr.com/photos/usnistgov/5940503177/` (accessed on May 20th, 2019)

[16] J.R. Martín-Solís, A. Loarte, M. Lehnen, *Formation and termination of runaway beams in ITER disruptions*, Nuclear Fusion, 57, 2017

[17] J.R. Martín-Solís, EUROfusion TS Ref. No. PMI-5.3.2-T008, *2018 TS activities on Runaway electrons: Modelling (0D and 1D) of runaway electron formation in DEMO disruptions*, 2018

[18] J.H. You, G. Mazzone, E. Visca, Ch. Bachmann, E. Autissier, T. Barrett, V. Cocilovo, F. Crescenzi, P.K. Domalapally, D. Dongiovanni, S. Entler, G. Federici, P. Frosi, M. Fursdon, H. Greuner, D. Hancock, D. Marzullo, S. McIntosh, A.V. Müller, M.T. Porfiri, G. Ramogida, J. Reiser, M. Richou, M. Rieth, A. Rydzy, R. Villari, V. Widak, *Conceptual design studies for the European DEMO divertor: Rationale and first results*, Fusion Engineering and Design, Volumes 109–111, Part B, 2016, 1598-1603

[19] J.H. You, G. Mazzone, Ch. Bachmann, D. Coccorese, V. Cocilovo, D. De Meis, P.A. Di Maio, D. Dongiovanni, P. Frosi, G. Di Gironimo, S. Garitta, G. Mariano, D. Marzullo, M.T. Porfiri, G. Ramogida, E. Vallone, R. Villari, M. Zucchetti, *Progress in the initial design activities for the European DEMO divertor: Subproject "Cassette"*, Fusion Engineering and Design, Volume 124, 2017, 364-370

[20] `https://www.researchgate.net/figure/CAD-models-of-a-single-cassette-of-the-54-units-in-the-ITER-W-divertor-and-exploded-view_fig1_315437873` (accessed on May 20th, 2019)

[21] P.A. Di Maio, P. Arena, G. Bongiovì, P. Chiovaro, A. Del Nevo, M.L. Richiusa, *On the thermo-mechanical behavior of DEMO water-cooled lithium lead equatorial outboard blanket module*, Fusion Engineering and Design, Volume 124, 2017, 725-729

[22] A. Del Nevo, E. Martelli, P. Agostini, P. Arena, G. Bongiovì, G. Caruso, G. Di Gironimo, P.A. Di Maio, M. Eboli, R. Giammusso, F. Giannetti, A. Giovinazzi, G. Mariano, F. Moro, R. Mozzillo, A. Tassone, D. Rozzia, A. Tarallo, M. Tarantino, M. Utili, R. Villari, *WCLL breeding blanket design and integration for DEMO 2015: statusand perspectives*, Fusion Engineering and Design, Volume 124, 2017, 682-686

[23] G. Maddaluno, G. Maruccia, M. Merola, S. Rollet, *Energy deposition and thermal effects of runaway electrons in ITER-FEAT plasma facing components*, Journal of Nuclear Materials, 313–316, 2003, 651–656

[24] `https://freefem.org`

[25] A. Ferrari, P.R. Sala, A. Fassò, J. Ranft, *FLUKA: a multi-particle transport code*, CERN 2005-10, INFN/TC_05/11, SLAC-R-773, 2005

[26] G. Battistoni, S. Muraro, P.R. Sala, F. Cerutti, A. Ferrari, S. Roesler, A. Fassò, J. Ranft, *The FLUKA code: Description and benchmarking*, AIP Conference Proceeding 896, 2007, 31-49

[27] G. Maddaluno, EUROfusion TS Ref. No. PMI-5.3.2-T016-D001, *Use of the FLUKA code for the evaluation of volumetric loads due to Res (Runaway Electrons)*, 2019

[28] E.N. Sieder, G.E. Tate, *Heat transfer and pressure drop of liquids in tubes*, Ind. Eng. Chem., 28, 1936, 1429–1435

[29] W.M. Rohsenow, *Heat transfer with evaporation*, Proc. Heat Transfer—A Symposium Held at the University of Michigan During the Summer of 1952, 1953, 101–150

[30] J.G. Collier, *Convective Boling and Condensation*, 3rd ed., Wotton-under-Edge, Clarendon Press, 1994

[31] M. Dalla Palma, P. Zaccaria, *Heat Transfer in Flow Boiling Conditions for Swirl Tube Elements Customizing the ANSYS Software*, International ANSYS Conference, 2006

[32] Y.A. Çengel, *Termodinamica e trasmissione del calore*, McGraw-Hill libri Italia srl, 1998

[33] C. Ruset, D. Falie, E. Grigore, M. Gherendi, V. Zoita, K.-D. Zastrow, G. Matthews, X. Courtois, J. Bucalossi, J. Likonen, *The emissivity of W coatings deposited on carbon materials for fusion applications*, Fusion Engineering and Design, Volume 114, 2017, Pages 192-195

[34] P. Tolias, *Analytical expressions for thermophysical properties of solid and liquid tungsten relevant for fusion applications*, Nuclear Materials and Energy, 13, 2017, 42–57

[35] F.P. Incropera, D.P. Dewitt, T.L. Bergman, A.S. Lavine *Foundations of heat transfer*, 6th edition, John Wiley & Sons, 2007

[36] J.W. Arblaster, *Thermodynamic Properties of Copper*, Journal of Phase Equilibria and Diffusion, Vol. 36 No. 5, 2015

[37] `http://www.mmluvata.com/Documents/Oxygen-free%20copper%20and%20special%20alloy%20data%20sheets/Chromium%20Zirconium%20Copper_ENG.pdf` (accessed on April 3rd, 2019)

[38] F. Gillemot, E. Gaganidze, I. Szenthe, EUROfusion TS Ref. No. 1.2.1.02, *Material Property Handbook on EUROFER97 (2015-MTA)*

[39] I. Barin, *Thermochemical Data of Pure Substances*, pub. VCH, Weinheim, 1993

[40] `www.iapws.org/` (accessed on April 9th, 2019)